Ultra-compact grating-based monolithic optical pulse compressor for laser amplifier systems

Submitted in partial fulfillment of the requirements for

the degree of

in

Electrical and Computer Engineering

Chang Yang

B.S., Electrical Engineering (Optoelectronics), Tianjin University
M.S., Electrical and Computer Engineering, Carnegie Mellon University

Carnegie Mellon University
Pittsburgh, PA

December, 2016

© Copyright by Chang Yang 2016
All Rights Reserved

Acknowledgement

The past four and half years at Carnegie Mellon University have been both challenging and rewarding for me. It is a lifetime memory that I will never forget.

There are many people that I want to thank for their help and support. I want to give my first thanks to my advisor, Prof. Elias Towe, for his countless instruction and guidance. I feel so lucky to meet such a great mentor in both research and life. He is the first one that I will turn to when I encounter challenges in research, and he is always there to inspire me with new solutions. I will always remember the encouragement he gave me when I was at the darkest moment of my life. I want to thank him for his consolation and understanding, which helped a lot to get me back on track more quickly.

The staff at Pittsburgh Supercomputer Center (PSC) gave me a lot of help during my whole simulation process. Their responses to questions and solutions to problems have been exceptionally quick and accurate. I couldn't fulfill my work without assistance from them.

I want to thank my friends and colleagues at CMU: Xiaoyu Bai, Zhengkun Dai, Min Xu, Yu-Han Liang, Ellen Reifler and so many others. They are truly a group of the most talented and interesting young people with who I shared many memorable conversations, both useful and useless. I want to thank them for keeping me company and giving me help, no matter in good times or bad.

I feel so lucky to have my husband, Jinxu Bai, always by my side. Meeting you is the best thing that ever happens to me. I want to thank you for so many things, I don't even know where to start. No matter in health or sickness, no matter rich or poor, I will always love you and stand by your side. You have always been my rock, and I want to be yours, too.

I want to give a special thank you to my parents, for their love, protection, and support all along. I cannot find a better family to have been born into to have lived with. I do not blame you for your decisions, but it will always be a big regret for my whole life. My parents are the strongest people that I ever know. I wish I can make you proud. I miss you, dad.

I would like to extend my great gratitude to my dissertation committee members: Prof. James A. Bain, Prof. Hong Koo Kim, and Prof. David N. Lambeth. Their help and suggestions for my thesis were most valuable. I also want to extend my gratitude to Prof. Gianluca Piazza, who gave me valuable advice and suggestion on my prospectus work, although he was not able to come for my defense because of conflicting schedules.

The financial support for the work contained in this Ph.D. dissertation was provided by the Defense Advanced Research Projects Agency (DARPA (HR0011-15-1-0009)).

My thesis committee:

Prof. Elias Towe, Advisor

Prof. James A. Bain

Prof. Hong Koo Kim

Prof. David N. Lambeth

Abstract

Ultra-short and high-peak-power laser pulses have important industrial and scientific applications. While direct laser amplification can lead to peak powers of several million watts, higher values than these cannot be achieved without causing damage to the amplifier material. Chirped pulse amplification technique is thus invented to break this barrier. By temporally stretching pulses before entering amplifier, the pulse peak power is significantly reduced and thus becomes safe to be passed through the amplifier. After amplification, a compressor is used to recover the pulse width, and high-power ultra-short laser pulses are produced.

Chirped pulse amplification technology increases the pulse energy by transferring the damaging effects of high-peak power laser pulses from the vulnerable amplifier to a relatively robust compressor system. The compressor is therefore a crucial device for producing high peak powers. However, there are some major drawbacks associated with it. First, compressors in high-energy laser system are usually over 1 cubic meter in size. For many applications, this large and cumbersome size is a limiting factor. Second, compressors are sensitive to outside disturbances; a little misalignment can lead to failure of pulse compression process. Third, gratings with large uniformly ruled area are difficult to fabricate, which impose a limit on achievable peak powers and pulse durations of laser pulses through the use of conventional compressors.

In this project, we present a grating-based monolithic optical compressor that offers a way around some of the major problems of existing compressors. By integrating the key optical components, one can make a robust and monolithic compressor that requires no alignment. In the new scheme, folding the optical path with reflective coatings allows one to design a compressor of significantly reduced size by minimizing both the longitudinal and transverse dimensions of the device. The configuration and operation mechanism of this novel compressor are described. A method for calculating the volume of the compressor is investigated. This is validated by computing the size of a specific monolithic compressor. Simulation results obtained through finite-difference time-domain method are presented, proving that the new compressor provides a compact, portable, and robust means for temporally compressing long duration pulses.

Table of Contents

Contents

List of Figures

List of Tables

1. Introduction and background

In this Chapter, the background and qualitative operation mechanism of the optical compressor, as well as chirped pulsed laser amplification technique, and where optical compressors are primarily used, are introduced. Major problems are identified, and solutions are proposed. Starting from Section 1.1, the development of the chirped pulsed laser amplification technique will be introduced, and then the operating mechanism and composition of chirped pulsed laser amplification system are explained. Section 1.2 demonstrates common compressor working mechanism by using a Treacy type compressor as an example. The disadvantages of the common compressor structure are summarized, and several efforts to improve the compressor in recent years are discussed. Finally in section 1.3, the objectives of this thesis are given, and a novel monolithic compressor is proposed to provide a solution to the existing problems in compressor design.

1.1 Chirped pulse laser amplification technique

In the 1950s, application of radar technology in the military made urgent the need to extend the ranges at which objects should be detected. In 1959, Charles E. Cook [1] investigated this problem and came up with a solution called “pulse compression”. In this radar regime dilemma, research scientists were faced with the fact that the transmitting tube peak power limitation for narrow pulse operation is usually reached before the full average power capability of the tube is realized. This limitation causes the transmission tube to be under used, and yet transmission is not efficient enough.

Employing the pulse compression technique, the average power available to illuminate radar target is increased without any loss at the receiver. This is accomplished by transmitting a wide stretched pulse through the transmission tube, and then temporally compressing the received signal to a much narrower pulse of high effective peak power. In this way, large peak power pulses are transferred outside the transmission tube to the receiver stage, and the transmitted signal is largely increased. The concept here to transfer the high power signal outside power sensitive element is highly intelligent and creative, and it provides the foundation of the chirped pulse laser amplification idea.

In 1968, E. B Treacy [2] implemented the world's first optical pulse compressor. In this experiment, an optical grating pair is used for direct pulse compression. Later in 1969, Treacy [3] quantatively analyzed his experiment and developed the initial theory for the grating compressor. This was the first time that the concept of an optical compressor was proposed. In 1984, Martinez et al. [4] reviewed the physics of the grating pair compressor, and discovered that angular dispersion was the key element that influences compressor performance. The Martinez review revealed the nature of the pulse compression technique. He also proposed a new perspective which suggested that a telescope be placed between the refracting optical grating elements to either obtain a larger negative dispersion in smaller geometry or to control the sign of group velocity dispersion [5]. Later on this configuration has been widely used as a matching stretcher to be paired with grating compressor.

While direct pulse compression can lead to ultra-short laser pulses, the achievable pulse energy is still limited by the nonlinear effect, or even damage to the amplifier material. In 1985, inspired by the previous solution of the same problem in radar, Strickland and Mourou [6] experimentally built the world's first chirped pulsed laser amplification system. In this experiment, a single mode fiber was used as the stretcher, while a grating pair was used as the matching compressor. The initial low-power short pulses are temporally stretched before entering amplifier. Thus the peak power of the pulses is largely reduced and it becomes safe to pass them into the amplifier. After amplification, the compressor temporally compresses the pulses back to their initial duration, and clean high-power pulses are safely produced. Their system produced laser pulses with pulse widths of ~2 ps and energies at the milli-Joule level. But it is difficult to move the single stage compressor compression ratio beyond 300 [7] with such a stretcher-compressor embodiment. This is because of the mismatch of linear positive dispersion provided by single-mode fiber and nonlinear negative dispersion generated by grating-pair compressor. In order to push the compression ratio, as well as achievable laser power forward, a perfect matching stretcher-compressor pair is essential. After recognizing this principle, modern chirped pulsed laser amplification systems capable of generating high-power ultra-short pulses usually employ a Martinez stretcher [5] and a corresponding Treacy compressor [3].

There are usually four parts in a chirped pulse amplification system: (i) an oscillator, (ii) a pulse width stretcher, (iii) an amplifier, and (iv) a compressor (Figure 1.1). The oscillator provides initial short, low power laser pulses. These short pulses are temporally stretched to have broad pulse widths by passing them through the stretcher. With the total energy of a single pulse unchanged due to energy conservation, the peak power of the pulses is significantly reduced. Thus it becomes safe for the pulses to pass through the amplifier so that the amplified pulses do not cause pulse distortion or damage to the amplifier material because of their reduced amplitudes. After different wavelength components of the pulse have been amplified independently in the amplifier, the pulse maintains its stretched width but with much higher peak power. In the next stage, the compressor compresses the pulse widths to their original width and thus ultra-short high-peak-power pulses are produced.

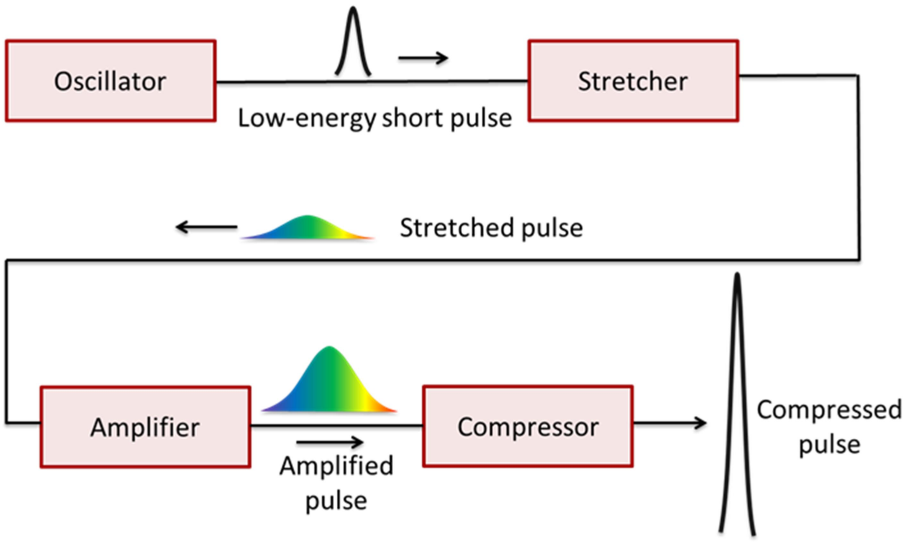

Figure 1.1 Chirped pulse laser amplification system.

By utilizing this technique, optical pulses with higher peak powers can be achieved without pulse distortion or damage to the laser components. The chirped-pulse amplification technique has undergone much refinement over the years. It is now capable of producing pulses with peak power levels in the terawatt range and pulse widths in the femtosecond regime [8-10]. It is obvious that the chirped pulse laser amplification technique accomplishes the task of boosting the laser power by transferring the high-power laser damaging effects from the usually vulnerable amplifiers to relatively more robust compressor part. Thus the compressor is the crucial part that defines the performance of chirped pulse laser amplification systems.

1.2 Optical pulse compressor

1.2.1 Common configuration and operation mechanism

The compressor is the crucial part in a chirped pulsed laser amplification system that is responsible for sustaining high-power laser pulses. It can be made from a fiber [11-15], fiber Bragg grating [16-18], prism [19], or a grating pair [2, 3, 6, 8-10]. Although fiber has the most compact volume compared to the other choices, it usually cannot be used as a compressor in high power laser systems. But for low energy systems, fiber, especially fiber Bragg grating, is a good solution for compact laser systems. Prisms can be used as compressor, too. But they are usually very large in size, and have a not-so-competitive dispersive ability. So it is very rarely used nowadays. The most widely adopted compressor configuration is parallel gratings, i.e., Treacy type compressor (Figure 1.2(a)), because of its superior power sustaining ability.

The stretcher and compressor always come in a pair, meaning that they should match with each other precisely to cancel out dispersion, so clean pulses can be produced. Commonly used stretchers include single-mode fiber [6], chirped Bragg fiber grating [20] and grating pair [8-10]. Among these choices, the fiber is undoubtedly the most compact one, and it is the most fragile one at the same time. For a stretcher, since the laser pulses are relatively low power, the requirement of robustness is not very critical. So fiber is widely used as stretcher for systems that do not have strict requirements on pulse shape and power scaling. The fiber Bragg grating has been investigated and used as stretcher in recent years. It can be designed to have flexible dispersion profile, so it does not have the mismatching problem that is common to single mode fibers. The only obstacle that keeps it from being widely adopted is its expensive price. After all, the most commonly used stretcher is grating pair with a telescope mounted between them (Figure 1.2(b)). The Strickland stretcher is chosen because it perfectly matches the Treacy compressor and it makes for an easy control of positive group velocity dispersion.

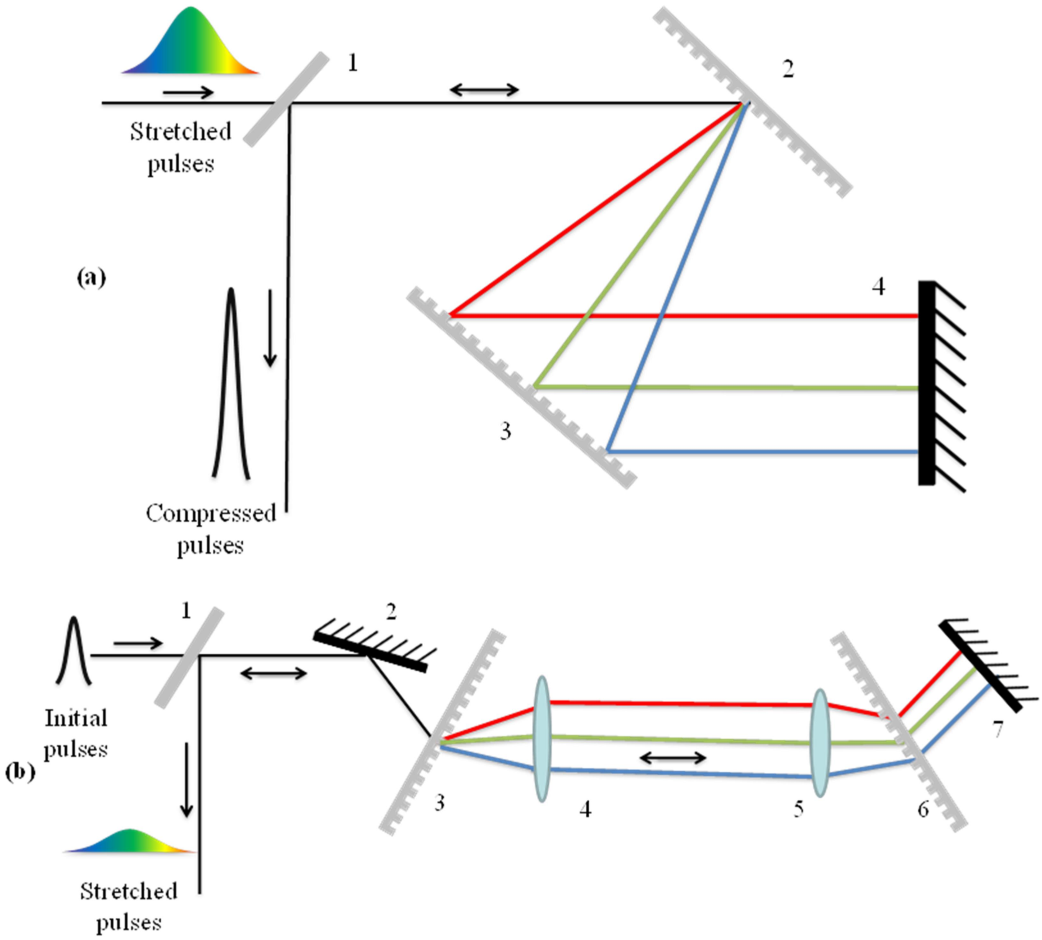

Figure 1.2 (a) A typical compressor setup. 1, one way mirror; 2 and 3, grating; 4, mirror reflector. (b) A typical stretcher setup. 1, one way mirror; 2 and 7, mirror reflector; 3 and 6, grating; 4 and 5, lens. The blue lines represent the shortest wavelength component; the red lines stand for the longest wavelength component; and the green lines are the medium wavelength component.

As shown in Figure 1.2 (a), the main body of common compressor is composed of two parallel gratings. We can see from the top view that these two gratings are mounted such that their rulings are parallel to each other. The first grating in the compressor serves the function of refracting (dispersing) the laser beam. The input laser pulses have a chirped profile where longer wavelength components come in earlier than the shorter wavelength components. Upon hitting the first grating, different wavelength components are refracted (dispersed) at different angles toward the second grating which re-collimates the beam into parallel light and fixes its angular dispersion at a given value. The mirror in the back end is perpendicular to the input beam direction, and it reflects input pulses back to their initial point following the same path they came in. After a round trip, the rear spectral components of the pulse catch up with the front ones by travelling a shorter optical path, causing the pulse to be compressed.

The common stretcher (Figure 1.2 (b)) is composed of the same grating pair as the compressor, with a telescope mounted between them. Note that here the two gratings are no longer parallel to each other. The core mechanism that the stretcher operates in is still optical path difference between different wavelength components, with the only difference being inverting the sign of group velocity dispersion compared to the compressor. The telescope serves this function by inverting the sign of the effective optical path. Between the two focal planes of the telescope, the effective optical paths for beams traveling at different angles are always the same. This length is thus subtracted from the total length traveled by the angularly dispersed beam, causing the effective optical path to be negative. After a round trip in the stretcher system, the initial chirp-free transform limited pulse obtains a positive chirp, and a stretched pulse with longer wavelength component traveling in the front can be produced. By adjusting the distance between the gratings and lenses, different amount of dispersion can be achieved to match the compressor.

This stretcher and compressor embodiment provides precise dispersion control, but for high power laser systems, the gratings that compose the compressor are usually over 1 meter square in size. In fact, there are three major drawbacks associated with the compressor. First, because of the principle of operation of the compressor, the highest achievable laser peak power and shortest pulse duration are determined by the available gratings, which must be uniformly ruled over large areas. Since it is difficult to fabricate gratings with large sizes, this imposes a limit on the peak powers and pulse durations achievable through use of conventional compressors. Second, large aperture compressors make it difficult for the laser systems to be implemented outside the laboratory, or in industrial settings where portability is often essential. Third, the cumbersome structure and alignment complexity of the compressor make it sensitive to external disturbances. Environmental changes can easily cause optical component displacement, thus making the compression process unsuccessful. These issues represent challenges that hamper advances in the state-of-the-art of high peak power, short pulse laser systems. Concerted effort has therefore been put into reducing the size and complexity of the compressor system. Concerted effort has therefore been put into reducing the size and complexity of the

compressor system. The two most representative examples of these efforts include using a fiber compressor [21-23] and folding the optical path in the compressor [24-26].

1.2.2 Approaches to reducing compressor size

a. Fiber compressor

Fiber is obviously the most compact choice. However, since the compressor is the component in CPA system that sustains the highest power passing through it, a fiber, used as compressor cannot survive the high peak powers after amplification [21]. For stretchers, however, a fiber with fiber Bragg gratings, is a good solution for compact laser systems [20].

In the earliest experiments, a single mode fiber was used as the stretcher to match a grating pair compressor [27]. This single mode fiber temporally stretches the pulses by the combined effects of dispersion and self-phase modulation. It is very difficult to control these two effects precisely [28]. However, nonlinearly chirped fiber Bragg gratings can be used to resolve this problem [20].

A fiber Bragg grating is formed by making a periodic modulation of the core refractive index over a certain length. The periodic nature of the index modulation translates into a resonant response, and the fiber Bragg grating reflects light at the Bragg wavelength defined by:

$$\lambda = 2 n_{eff} \Lambda, \tag{1.1}$$

where n_{eff} is the average effective index of the fiber and Λ is the local period of the grating.

A grating with a modulation period that varies along the fiber axis reflects light of different wavelengths at different positions. For example, a chirped fiber Bragg grating with a linear period profile generates a group delay that varies linearly with wavelength. Figure 1.3 illustrates a pulse stretched by a chirped Bragg grating with a period that decreases away from the entrance point. Longer wavelengths are reflected early at the beginning while shorter wavelengths are reflected later near the back. The spectrum of the pulse is dispersed temporally, resulting in a stretched output pulse.

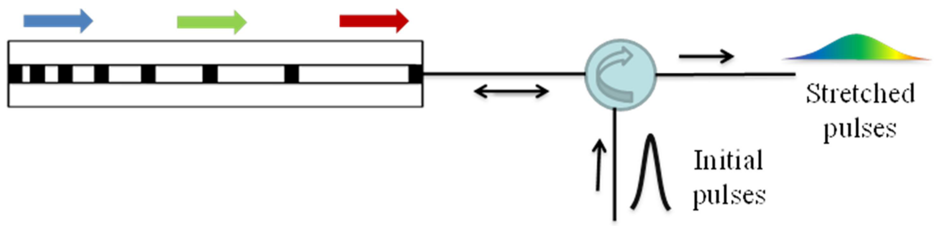

Figure 1.3 Chirped fiber Bragg grating.

Different modulation profiles can be realized to generate various spectral dispersions. The modulation amplitude of the fiber Bragg grating can be tailored as well to spectrally shape the grating reflectance. In theory, any dispersion profile can be achieved using nonlinearly chirped fiber Bragg gratings. Since the stretcher can be designed flexibly, we can design it to match the compressor dispersion profile after we confirm the compressor parameters. In the future, after fabrication and experimentation with the designed compressor, a matching fiber stretcher will then be designed.

b. Folding the optical path

Another approach to reducing compressor size is to fold the optical path. This method usually includes several additional optical components and requires complicated alignment [25]. A simple example to fold the compressor utilizes two roof-mirror reflectors [26] (Figure 1.4). By utilizing this structure, one grating is eliminated from the compressor.

To understand how this system works, we need to examine the top view (Figure 1.4(a)) and front view (Figure 1.4(b)) of this system. A laser beam is incident onto the grating at a certain height with respect to the optical axis of roof mirror 3, but in the same level with roof mirror 2. The grating refracts the beam towards roof mirror 2, and the beam gets retro-reflected with a lateral displacement. The beam is refracted by the grating again, and directed towards roof mirror 3. The roof mirror reflects the beam back into its direction with a small vertical displacement. The beam repeats the same propagation procedure in this translated space, and finally comes out of the compressor system with a compressed profile. Thus the input pulses will hit the grating four times, which is exactly the same as with the Treacy compressor. Shown in Figure 1.4(a) is the complete optical path of the beam, with the input and output paths overlapping with each other. The only difference between them is a vertical displacement caused by the roof-mirror reflector.

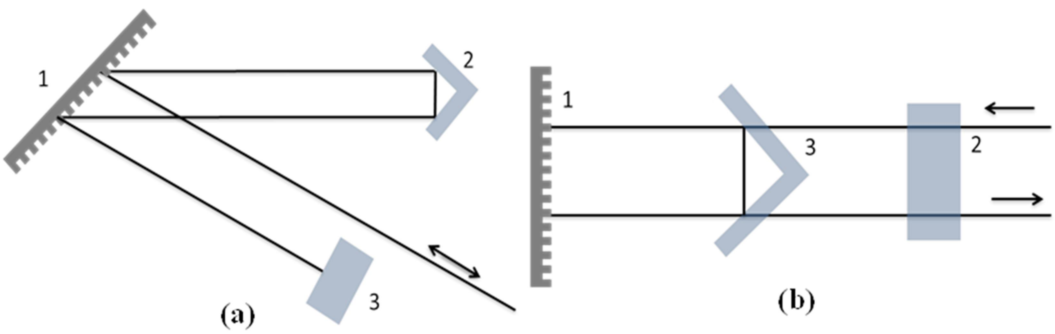

Figure 1.4 (a) Top view of the folded compressor. (b) Front view of the folded compressor. 1, grating; 2, roof-mirror reflector for horizontal displacement; 3, roof-mirror reflector for vertical displacement.

Similar to the structure above, the folded compressor in Reference [25] involves an additional roof mirror to yield a six mirror assembly. Even after this folding effort, the footprint of the whole system is still $3m \times 0.7m$. In conclusion, although the folding optical path method is able to reduce the compressor size, it is fragile and cumbersome due to the additional number of optical elements. Alignment of the folded system is complicated, and the beam quality can be significantly impacted by any small disturbance or movement of the system.

As discussed in the previous section, a nonlinearly chirped fiber Bragg grating can be used as a stretcher to match different kinds of compressors because the Bragg grating profile can be designed with different profiles to compensate for the negative dispersion that the compressor imposes on the pulses. But for the compressor, fiber is too fragile to damage and cannot be used as a compressor choice for high power laser systems. The only choice left is the grating compressor. However, folding the optical path is also not good enough as it does not result in a compact or robust compressor. So we need to think of another way to reduce the compressor size, and at the same time making the system robust and portable. This is my major topic and I will introduce how I accomplish this task in the following sections.

1.3 Thesis statement and contribution

In this thesis, a compact and robust compressor for portable high-power laser system is designed, computed and simulated. We present a grating-based optical compressor that offers a way around some of the major problems of existing compressors. By integrating the key necessary optical components, one can make a robust and monolithic compressor that requires no alignment. In the new scheme, folding the optical path with reflective coatings allows one to design a compressor of significantly reduced size by minimizing both the longitudinal and transverse dimensions of the device. This new compressor is differentiated from the traditional one by its drastic reduction in size of the gratings required to implement it; grating size has generally been a limiting factor to portability and scaling of power handling capabilities of some laser systems. When paired with properly designed nonlinearly chirped fiber Bragg gratings in them, it becomes feasible to make robust and compact pulsed laser amplification systems.

The compactness of the designed compressor is proved theoretically through volume calculation. The two methods of group velocity dispersion analysis, Taylor series expansion and ray tracing, are investigated and compared. Due to the unique nature of the monolithic compressor design, a modified ray tracing method is finally conceived to calculate its volume. The computational results obtained for the novel monolithic compressor and Treacy compressor are compared, and the novel compressor is proved to have a reduced volume compared to the traditional one.

A simulation program based on the finite-difference time-domain method is developed to simulate the response of the designed compressor to a chirped long Gaussian pulse. The output pulse is extracted and analyzed. The pulse is successfully compressed as predicted by previously developed theory, with a small dent in the middle caused by a discontinuous change of the optical path length. This can be reduced by making the resolution finer, or making the designed compressor to have a more folds for transverse size reduction.

2. Novel compressor design

A practical compact compressor design comes from the base of properly using pulse compression theory. In this chapter, the configuration and qualitative operation mechanism of novel monolithic compressor are described, following the compact compressor design guideline concluded from pulse compression theory. In section 2.1, the core theory behind pulse compression technique is first explained, followed by the design guideline for compact compressors concluded from this theory. In section 2.2, the proposed simple version monolithic compressor configuration and qualitative operation mechanism are introduced, while the configuration and qualitative operation mechanism for advanced version are explained in section 2.3. The major difference between these two versions is that the simple version only reduces the longitude size of compressor, while the advanced version also reduces the transverse size (the grating size). The simple version can be treated as a reduced case of advanced version where only robust configuration is essential. Therefore in the following chapters, when we mention about the novel monolithic compressor, we are referring to the advanced (full) version compressor. In section 2.4, the advantages of the monolithic compressor are concluded and compared to the traditional ones.

2.1 Optical pulse compression theory – general perspective

2.1.1 Angular dispersion

Group delay is defined as the time it takes a light pulse to travel a unit distance, and group velocity is the inverse of the group delay. A pulse with finite bandwidth will experience what is called group velocity dispersion. That is to say, different wavelength components will have different group velocities. A simple example of group velocity in a dispersive medium can be expressed as:

$$v_g = \frac{d\omega}{dk} = \frac{c}{\left[n + \omega\left(\frac{dn}{d\omega}\right)\right]}. \tag{2.1}$$

From the equation above, we see that the origin of the dispersion phenomenon is the different refractive indexes for the different frequency or wavelength components of light. Of course this is only one situation where group velocity dispersion is caused by material dispersion. In other cases group velocity dispersion can also be caused by angular dispersion (for example, diffraction caused by angular spread-out or modal dispersion and waveguide dispersion in waveguide). In any case, group velocity dispersion is the reason different frequency or wavelength components in light pulses get spread out in time, causing the pulses to be temporally stretched or compressed.

The stretching and compressing phenomena are caused by group velocity dispersion. The main source of group velocity dispersion in compressors is angular dispersion [4]. It is negative irrespective of the sign of the material dispersion, and it can be devised so that it can dominate group velocity dispersion. The larger the angular dispersion is, the higher the compression ratio a compressor can have. We will demonstrate why this is the case with the following derivation.

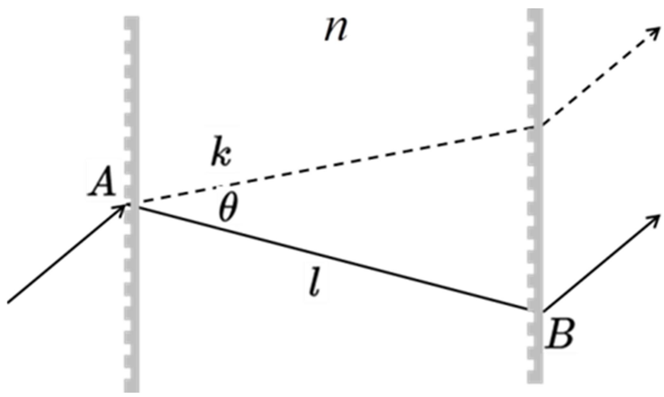

Figure 2.1 A two-grating structure.

Consider the typical compressor structure shown in Figure 2.1. The refractive index of the material in the space between the two gratings is n. A and B are two randomly chosen points in the two grating planes. The dashed line represents the actual direction of the wave vector $\vec{k}$; θ is the angle between the actual wave direction and the line of reference AB; and l is the distance between A and B. Assume that the incident wave is a plane wave. The phase delay $\emptyset$ suffered by the wave refracted with a wave vector $\vec{k}$ between the points A and B will be given by the scalar product of vector $\vec{k}$ and $\overrightarrow{AB}$:

$$\phi = \vec{k} \cdot \overrightarrow{AB}. \qquad \textbf{(2.2)}$$

The equivalent optical path P is expressed by:

$$P = \phi c / \omega = nl \cos\theta, \qquad \textbf{(2.3)}$$

where c is the velocity of light, and ω is the angular velocity of the light in the medium.

The second-order term in the expansion of the phase shift in powers of the frequency gives the net group-velocity dispersion:

$$\frac{d^2\phi}{d\omega^2} = \frac{d^2\omega P / c}{d\omega^2} = \frac{\lambda^3}{2\pi c^2} \frac{d^2 P}{d\lambda^2}, \qquad \textbf{(2.4)}$$

where λ is the wavelength of light in the medium.

With the coefficient being a constant, it is clear that the group velocity dispersion solely relies on the second derivative of P, which can be obtained from equation (2.3) as:

$$\frac{d^2P}{d\lambda^2}=l\cos\theta\frac{d^2n}{d\lambda^2}-2l\sin\theta\frac{dn}{d\lambda}\frac{d\theta}{d\lambda}-nl\cos\theta\left(\frac{d\theta}{d\lambda}\right)^2-nl\sin\theta\frac{d^2\theta}{d\lambda^2}. \quad \textbf{(2.5)}$$

If the reference line $\overrightarrow{AB}$ has the same direction as $\vec{k}$, the equation above will reduce to:

$$\frac{d^2P}{d\lambda^2}=\left[\frac{d^2n}{d\lambda^2}-n\left(\frac{d\theta}{d\lambda}\right)^2\right]l. \quad \textbf{(2.6)}$$

The contribution to the group-velocity dispersion of the second term is always negative irrespective of the sign of the material dispersion. This term is called the angular dispersion. Angular dispersion is the main source of group-velocity dispersion in compressors, causing compressors composed of two parallel gratings to have negative dispersion. To achieve a large difference in optical path for different wavelength components, different wavelength components should be refracted far away from each other in a long distance. Thus large gratings mounted far apart from each other are needed to achieve high compression ratios. This is the main reason that has made recent high power ultra-short chirped pulse amplification laser systems to be so large.

2.1.2 Compressor design guideline

My goal in this project is to reduce the compressor and stretcher system sizes as much as possible, while keeping them robust enough to be portable. Given the fact that the key to the compression technique is to have large angular dispersion, large dispersion angles and long effective optical paths become the two essential elements required for achieving a high compression ratio. Since the grating is the most dispersive element until now [29], it needs to be the refractive element. The only feature we can change is the effective optical path. So what I need to do is to rearrange the compressor geometry to obtain large angular dispersion in limited space.

The longitude size of the compressor, as stated in the angular dispersion equation, is inversely proportional to the refractive index of the material in between the two gratings that compose the compressor. So it can be reduced by inserting material with higher refractive index than that of air. Another benefit comes along with inserting high refractive index material is that all the optical elements in the compressor can be integrated, thus making compressor a monolithic device that is robust and no longer sensitive to outside disturbance. Inspired by this, in section 2.2, the simple version monolithic compressor is proposed. It reduces the longitude compressor size by inserting fused silica material between the gratings, and it becomes an integrated device that needs no more alignment.

The tricky part is reducing transverse size, or more specifically, the grating size of compressors. The lack of gratings with large uniformly ruled area is the major problem that hinders the development of chirped pulse laser amplification systems.

Reducing grating size will not only lead to reduced size of existing chirped pulse laser amplification system, but can also boost the achievable power of the system to another level.

In the traditional compressor structure, the first grating that serves the function of refracting light can be small. It only needs to be large enough to take in all the input light (or in other words, larger than the input beam spot size). So it is not the problem. But the second grating must be large, because different wavelength components are refracted at different angles according to grating equation, and each wavelength component in the input light needs to intersect with the grating in order to be re-collimated. So each wavelength component has a unique intersecting point with the second grating which is not shared with others, and the widely spread optical beam leads to large grating size. Consider in a compressor system where transmission type fused silica gratings are used, energy received on unit area is far below the damaging threshold of the given grating. This is a waste of the grating power scaling ability.

To reduce the size of the second grating in compressor, the advanced version of monolithic compressor is proposed in section 2.3. In this embodiment, reflective coatings are added on sides of the fused silica block in between the gratings, which serves the function of folding the beams back into the block until they reach at the second grating, and the grating size (or transverse size) is therefore reduced. Moreover, this folding mechanism forces different wavelength components separated for a certain distance to share the same intersecting point on the second grating, which makes better use of the grating power scaling ability.

This advanced version compressor provides a better solution to our request of compact and robust compressor configuration compared to the simple version. Thus in the chapters after this one, when we mention novel monolithic compressor, we are referring to this advanced version, or full version. The simple version is a reduced case of the proposed monolithic compressor where transverse size reducing feature has not been added.

2.2 Novel compressor structure – simple (reduced) version

2.2.1 Device configuration

Figure 2.2 is the embodiment of the simple version of a monolithic compressor. It is comprised of three solid and optically transparent blocks (1, 2, 3) with an index of refraction that is larger than that of air. For practical reasons and for the sake of the discussion, we assume that the blocks are fused silica from now on, for both the simple and advanced version of monolithic compressors.

The light grey colored parts represent fused silica material, and the parts colored in green stand for reflective coating. The coating can either be metal (such as gold) coating or distributed Bragg reflector. In this simple version, since all the wavelength components are reflected for a same number of times, half-wave loss is not a concern. Thus metal coating is a better choice based on its ease of fabrication and less design complex. The simple version can be understood as a special case of the advanced (or general) version, where reducing grating size is not an urgent request.

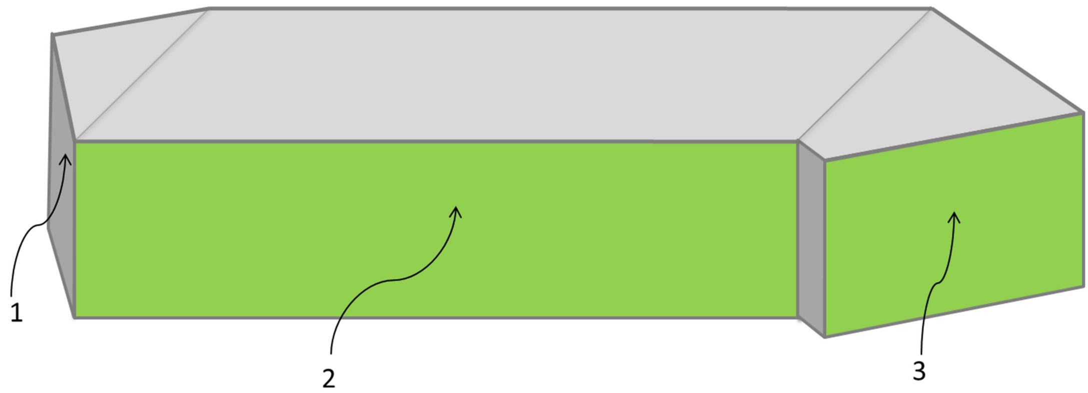

Figure 2.2 A 3-D drawing of the designed simple version compressor.

Illustrated in Figure 2.3 is the first of the three blocks 1, which is a triangular prism with no special surface features. Figure 2.3 (a) shows the 3D projection of block 1 with its surface that is attached to block 2 exposed. The top and bottom surfaces of this block are exactly the same, and they are both right triangles. The other three side surfaces are rectangles in different sizes. The dashed red arrow indicates the input source light, and it is impinging on the rectangle that is not visible in this 3D projection.

Seen from the top, with the surface touching block 2 shown as the vertical line, block 1 is a right triangle (Figure 2.3 (b)). The angle at the vertice that does not touch Block 2 is 90 degrees. The other two angles of the top and bottom triangles depend on the desired dispersion. The input light is indicated with the red arrow, and it is incident perpendicularly onto the input plane. The input plane (Figure 2.3 (c)) is a simple rectangle. For better performance, it should be covered with an anti-reflection coating. The red cross indicates the input point of source.

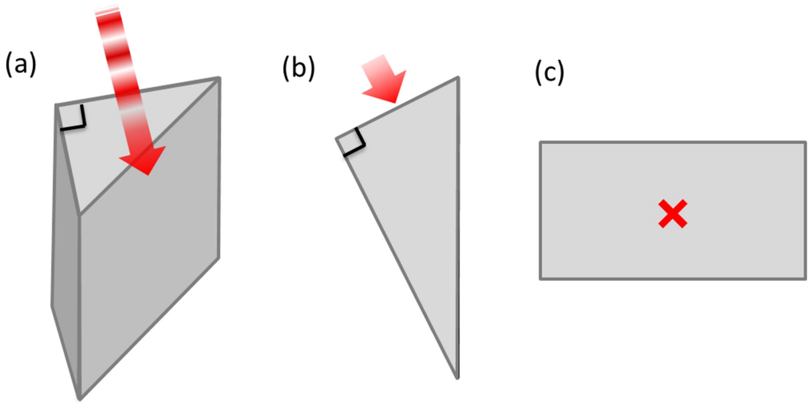

Figure 2.3 Left part of the designed simple version compressor. (a) 3D projection; (b) top view; (c) side view on the input surface.

Block 2 is shaped as a rectangular cuboid (Figure 2.4). Each of the opposite and parallel faces of the block labeled with fine lines, has a grating ruled on it. The other two surfaces of the block indicated with green color, are covered with a thin, perfectly reflecting coating. This coating can either be metal (such as gold) or distributed Bragg reflectors. The top and bottom surfaces (shown in light grey as fused silica) have no special surface features, because they will not interact with light anyway.

Figure 2.4 Middle part of the designed simple version compressor.

Bonded to block 2, at an angle of less than ninety degrees, at one of the surfaces with the second grating is the trapezoidal block 3 of Figure 2.2 (Figure 2.5 (a)). Different views or projections of block 3 are also shown to the right of it. The surface colored with green is covered with reflecting coatings, same as block 2. The light grey surfaces have no special feature.

The face that is opposite to the green one, and cannot be seen in Figure 2.5 (a), is joined to block 2. It is shown in the left view (Figure 2.5 (d)) of block 3 with the rectangle on the left. The top and bottom surfaces of block 3 have the same shape, and their shape is illustrated in Figure 2.5 (e). The face that is attached to block 2 is shown with the vertical line. The other two lines that have intersection with the vertical line are parallel to each other, indicating that the surfaces they are representing have the same relationship. The remaining line is perpendicular to both of these two lines, and this is the line that represents the surface that's covered with reflective coating. Taking the vertical line as it is pointing out of paper, we have the front view (Figure 2.5 (b)) and rear view (Figure 2.5 (c)) of block 3.

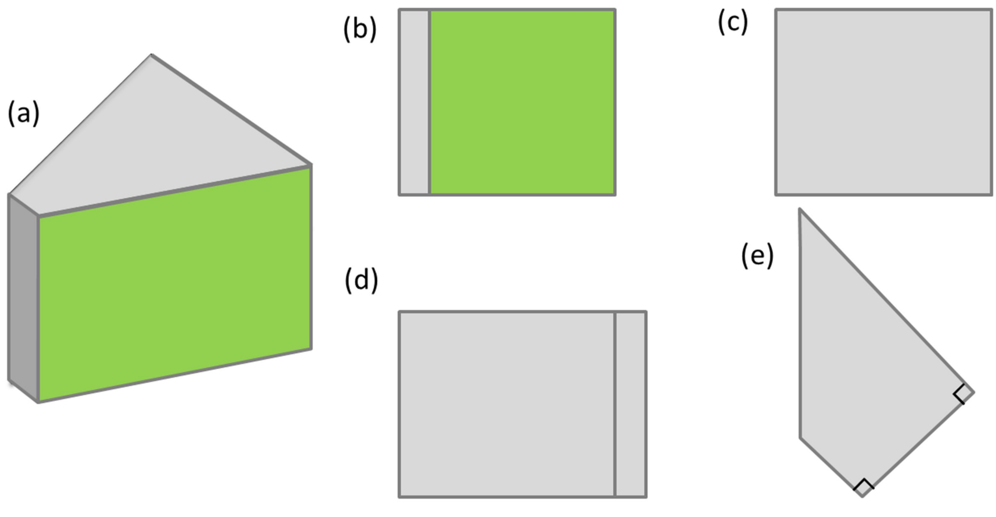

Figure 2.5 3-D drawing of the right part of the designed simple version compressor and its different views: (a) 3D projection; (b) front view; (c) rear view; (d) left view; (e) top view.

2.2.2 Operation mechanism

The top composite view of the new compressor is shown in Figure 2.6, with an illustration of how light propagates from the input at the left to the right of block 3, and back after retro-reflection from block 3 to the input of the compressor, which also serves as the output.

In operation, a train of stretched pulses enter the compressor from the left-hand side as indicated with the black arrow, impinging on the first diffraction grating ruled on the rectangular cuboid-shaped block 2. The light is then angularly spread by diffraction according to its spectral content, with the longest and shortest wavelength components following the paths indicated by red and purple lines, respectively.

Due to the limited transverse size of the solid block, light beams encounter the perfectly reflecting surfaces of the block and are thus folded back into the block for the same times. This process is repeated several times until the beams reach the second grating. Note that in this block, all the wavelength components are reflected the same number of times, and this number should be even (if the beams are reflected for an odd number of times, this structure can still work, but with the third part rotated by 180 degrees).

The second grating diffracts the beam, causing it to travel along a direction parallel to its original line of travel before it entered the compressor. These beams then propagate through the body of block 3 and encounter a perfectly reflecting surface perpendicular to the light direction of travel. Retro-reflection from this surface returns the light along the same path to the initial starting point. The returned beam is the output, with each pulse in the train of pulses temporally compressed to a much shorter width and higher amplitude than the original input pulses.

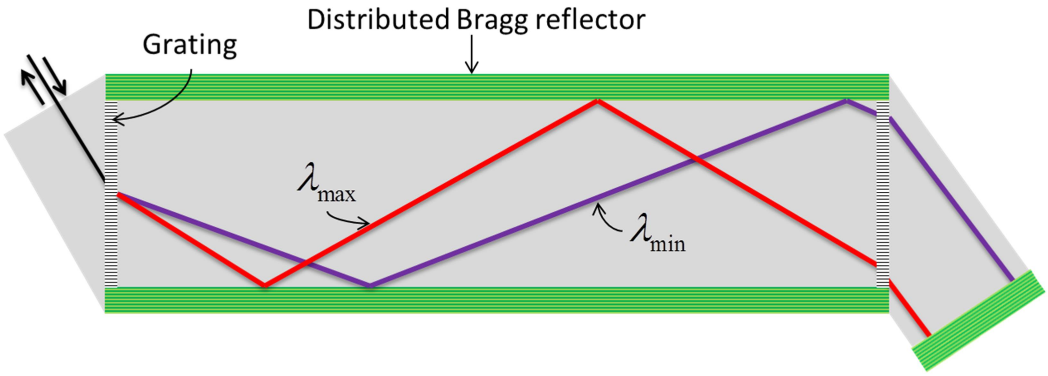

Figure 2.6 Beam propagation trace on top view of the designed simple version compressor.

In the whole process, the light beams hit on the gratings for four times, which is the same as Treacy compressor. The longitude size is reduced by inserting a material with higher refractive index than that of air, and the compressor becomes a monolithic block no longer sensitive to outside disturbance. The transverse size, however, has remained the same with traditional case. Essentially, this version of monolithic compressor has a similar operation mechanism with the traditional ones. So this simple version compressor is most useful where monolithic configurations are the primary concern. Here since our goal is to simultaneously reduce compressor size and to make a robust configuration, our major discussion will be focused on the advanced version. From here on when we mention novel monolithic compressor, we are referring to the advanced version, not this simple version.

2.3 Advanced (full) version of the monolithic compressor

2.3.1 Device configuration

Figure 2.7 is a geometrical illustration of the preferred embodiment of proposed monolithic compressor. It is comprised of three conjoined solid and optically transparent blocks (1, 2, 3) with an index of refraction that is larger than that of air. Here the material represented with light grey color is fused silica, while green stands for reflective coating.

There are four surfaces on this device that is covered with reflective coating: two on the central block labeled as 2, and two on the right most block labeled as 3. The coatings on block 2 must be distributed Bragg reflectors, because in this embodiment different wavelength components are reflected on the coatings for different number of times, and metal coatings will cause half-wave loss which is hard to account for. The coatings on block 3, however, can be either distributed Brag reflector or metal coating. This is because of the reason that all the wavelength components in the beam, no matter reflected by side reflectors (on block 2) for how many times, and no matter reflected by which reflector at the right most end (block 3), are only retro-reflected once. Since it is the same for all wavelength components, both metal coating and distributed Bragg reflector will serve the function in this block.

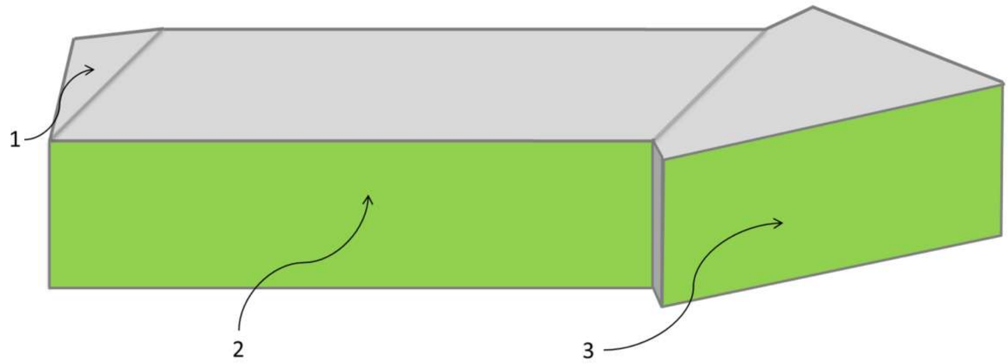

Figure 2.7 A monolithic three-dimensional compressor – advanced version.

Block 1 (Figure 2.8 (a)) is a triangular prism with no special surface features. It is attached to block 2 in a way that is illustrated in Figure 2.7. The rectangular surface exposed in Figure 2.8 (a) is joined with one of the gratings on block 2, and this surface conjunction is indicated in Figure 2.7 with the faded grey boundary line between block 1 and 2. Again, the top and bottom surfaces are the same right triangles, and the other three side surfaces are rectangles in different sizes. The dashed red arrow indicates the input light, and it is impinging on the side surface that cannot be seen in this 3D projection.

If we take the surface to be joined perpendicular to the principle plane, then the top view of this block 1 will be as shown in figure 2.8 (b). There is a corresponding triangle at the bottom. Both the triangles on the top and the bottom of this block subtend a 90-degree angle at one of the vertices that does not touch Block 2. The other two angles of the top and bottom triangles depend on the desired dispersion at the surface that is in touch with Block 2, and hence on the input angle of the beam.

The input beam (indicated with the arrow) is incident perpendicularly onto the input plane, which is the smaller one of the two rectangular side surfaces that are not joined to block 2. The location of the input beam is indicated on the input surface in Fig. 2.8 (c) with a cross. It does not have to be at the midpoint of that square surface, as long as it is somewhere in the upper middle or bottom edge of the surface. For the best performance, this plane should be covered with anti-reflection coating.

The purpose of this triangle prism block is primarily to balance the dispersion difference between air and fused silica material over the plane of grating. Moreover, it can also serve as the input locator for the whole device. One can therefore cover the rest of the plane surface in Fig. 2.8 (c) with an opaque material except for the input point.

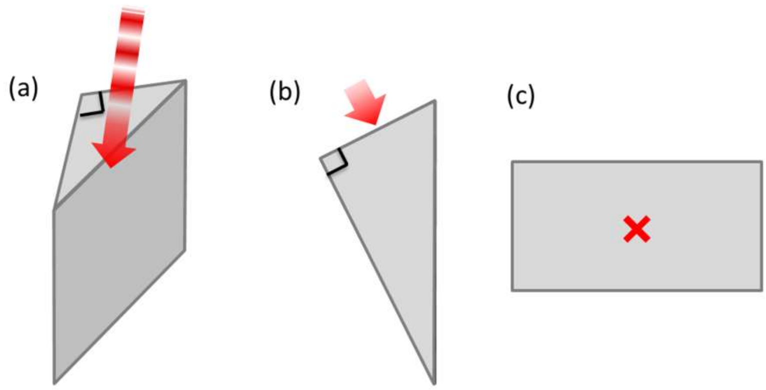

Figure 2.8 (a) Block 1 of monolithic compressor; (b) top view of Block 1; and (c) side view of the Block 1 from the input plane.

The majority of the monolithic structure is comprised of the cuboid Block 2, illustrated in Figure 2.7 and independently in Figure 2.9. Two of the opposing but parallel faces of Block 2, have a grating written on them. In this 3D projection, the left most surface, which cannot be seen in this illustration, is attached to block 1. The right most surface, which is exposed here with grating rulings, is attached to block 3 as illustrated in Figure 2.7.

For high-power laser systems, one important requirement is high damage threshold of the compressor, or to be more specific, of the gratings in the compressor. This is one of the reasons why transmission gratings are usually the preferred design option. Such gratings have a damage threshold that can approach that of bulk materials [29]. Unlike common gold-coated gratings whose damage threshold is about 1.5 J/cm^2, the damage threshold for fused silica transmission gratings is 2100 J/cm^2, and it is 4250 J/cm^2 for bulk fused silica material. The damage threshold of the monolithic structure is therefore only limited by the properties of the bulk material.

The front and rear surfaces of this block should be covered with a properly designed distributed Bragg reflector (illustrated as green here and in all the following figures). They serve the function of folding the light beams back into the block while traveling towards the second grating. The other two remaining surfaces can have no special surface feature, or to be more cautious, they can be covered with reflective coatings. In any case, it is immaterial since they are not involved in reflecting or transmitting signal light.

The reason for use of distributed Bragg reflectors instead of conventional reflecting coatings (which are easier and less expensive) is that different wavelength components need to be reflected at the (green) side surfaces of the block for different number of times. Perfectly reflecting metal coatings cause different wavelength components to experience different numbers of times of half-wave losses at the material interfaces. This makes it difficult to control and predict dispersion. Another beneficial aspect of using a distributed Bragg reflector is that it provides higher damage threshold than metal coating, which is what desired for a high-power purpose optical compressor.

Figure 2.9 Block 2 of monolithic compressor.

The third major component of the compressor, Block 3, is an irregularly shaped heptahedron shown in Figure 2.10 (a); different views or projections of it are illustrated alongside the three-dimensional isometric.

The areas shown in green indicate surfaces covered with reflective coatings (we will assume these are distributed Bragg reflectors from here on); light grey regions represent surfaces of fused silica without any special features. This block is attached to block 2 as indicated in Figure 2.7 with the faded grey boundary line. At this interface, the second grating of block 2 is joined to the surface of block 3 that is opposing the two reflective surfaces, which cannot be seen in the 3D projection of Figure 2.10 (a). This surface is illustrated in Figure 2.10 (d) (left view of block 3) with the rectangle in the middle.

Different views of block 3 are taken such that the conjunction surface to block 2 is considered the principal vertical plane. The front and rear views of this block (Figure 2.10 (b), (c)) are exactly the same because block 3 is symmetric with respect to the vertical central plane of block 2. Similarly, the left view of Block 3, illustrated in

Figure 2.10 (d), is symmetric with respect to a vertical central line. The square plane in the middle of this block attaches to Block 2.

The top view of block 3 is shown in Figure 2.10 (e), and is symmetric with respect to a horizontal central line. There are two right (90-degree) angles on this surface as indicated. Each of these, however, could be less than 90^{o} if there is a mechanical tolerance error involved. In Figure 2.10 (e), the angle to the right of the corners with the 90-degree angles should be less than or equal to 90 degrees to avoid laser beams overlapping. It is also a result of the glazing input angle. The two surfaces of block 3 that do not intersect with block 2 serve the function of retro-reflecting incident beams back into their original path; this means one of these two surfaces is perpendicular to the incident beam direction, and the other is mirror symmetry of the incident beam direction with respect to an axial line in block 2. The two surfaces must therefore be coated with properly designed distributed Bragg reflector structures. The remaining five surfaces of Block 3 have no special features on them.

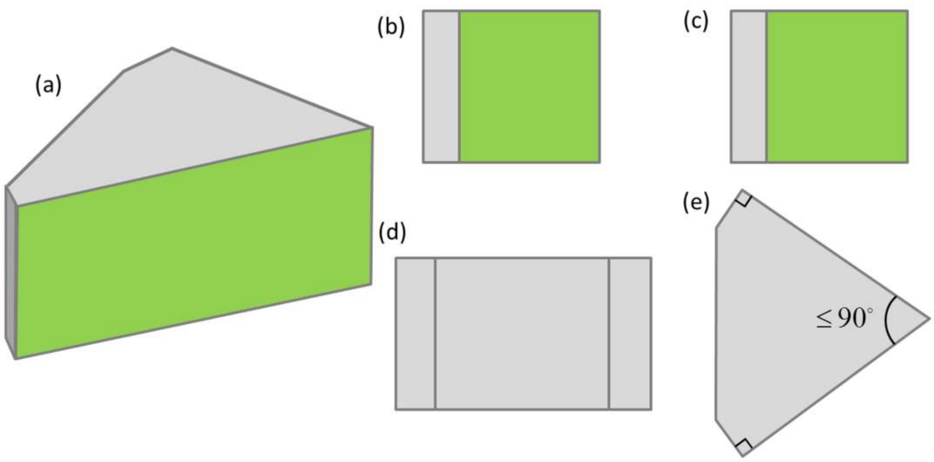

Figure 2.10 (a) Block 3 of the monolithic compressor; (b) front view of Block 3 and (c) the rear view of Block 3. (d) Left view of Block 3, and (e) the top view of Block 3.

One viable approach to fabricating the monolithic compressor is to begin with a fused silica Block 2 of the appropriate shape and desired dimensions. A pair of transmission gratings are then written onto two of the most widely separated opposite surfaces of the block, with the grating area covering the entire surface. As indicated in green in Figure 2.7, one then deposits distributed Bragg reflectors on the other set of opposite surfaces of Block 2. Finally, appropriately shaped and dimensioned blocks 1 and 3 are then atomically bonded [30, 31] to opposite sides of Block 2 as indicated in Figure 2.7.

2.3.2 Principle of Operation

The manner in which light propagates through the composite monolithic compressor is indicated in Figure 2.11; this illustration is of the top view of the structure. Since there are no refracting elements or reflecting effects in the axis that is parallel to grating rulings, the light field in vertical direction will not change in the whole compression process. Therefore this top view of the beam propagation trace contains all the necessary information we need to keep track of the compression process. Edges of the structure shown in green represent distributed Bragg reflectors; light grey is the interior of the fused silica, and yellow represents a metal (such as gold) coating. Note that this metal coating is optional. Here, the longest wavelength component of an input pulse is represented by the color red, while purple represents the shortest wavelength component.

In operation, a train of stretched pulses enter the compressor from the left-hand side as indicated; they impinge on the triangular prism in a direction that is perpendicular to the input surface as described previously. Because of reflection due to a refractive index difference between air and fused silica, this surface should be coated with an anti-reflection coating to minimize reflection. Inside Block 1, all wavelength components travel along the same path (as represented by the black line).

Upon transmission through the first diffraction grating, the beam is angularly spread by diffraction. The longest and shortest wavelength components follow the trajectories indicated with the red and purple lines, respectively. The light beams then encounter the distributed Bragg reflectors on the sides of block 2 and are folded back into the block; different wavelength components may be reflected for a different number of times before the beams reach the second grating. These components can be divided into two groups: one set is reflected for an even number of times, and the other for an odd number of times. Diffraction of light components at the second grating that are reflected for an even number of times by the distributed Bragg reflectors lead to retro-reflected light component that is parallel to the original input beam in Block 1; light components reflected by an odd number of times are diffracted at an angle that is a mirror symmetry of the incident beam with respect to the center line of Block 2.

These light components propagate through the body of Block 3, and are retro-reflected by the distributed Bragg reflectors at the edges of Block 3, which are perpendicular to the light direction of travel. Retro-reflection sends the components along the same path back to their original starting point in Block 1. The returned composite beam is the output, with each pulse in the train of pulses temporally compressed to a much shorter width than the original input pulses.

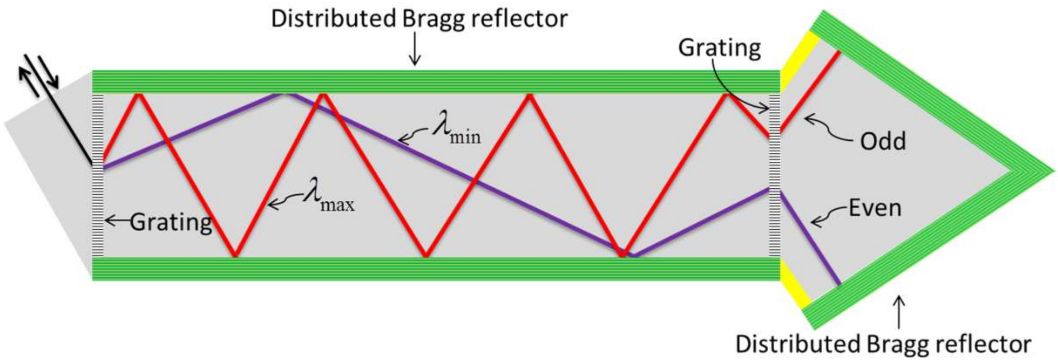

Figure 2.11 Trajectory followed by spectrally dispersed light as it propagates through fused monolithic compressor.

2.4 Advantages of the novel compressor design

Use of the three solid blocks on which the grating and reflection elements are integrated provides two key benefits. The first is a higher index of refraction than that of air between the gratings of the common compressor. This helps reduce the size of the compressor while retaining the same beam physics; the second benefit comes from the reflecting coatings on the side surfaces of the bonded blocks; the coatings provide a mechanism for folding the optical path length within a compact volume. The distinguishing advantage of this invention is its substantial reduction of the overall volume of the optical compressor, or to be more specific, the reduction of the gratings size needed. A secondary benefit is its robustness to minor mechanical disturbances and relative ease of alignment.

If tuning of the input angle is desired in some laboratory experimental implementations, the second block (Figure 2.9) alone can be used as the dispersive element. We could simply pair it with two mirrors serving the function of retro-reflecting beams coming out of the second grating, and their positions will change according to the changing input beam direction. This way input direction tuning can be accomplished. Or even in some cases, overall adjustment is needed all the time, a transverse size folded apparatus can still be accomplished by simply placing two broadband dielectric mirrors between the gratings to fold the transverse optical paths, and two other mirrors after the second grating to retro-reflect the beams.

To take full advantage of the compact, monolithic new compressor in chirped-pulse amplification systems, one should pair it with a non-linearly chirped fiber Bragg grating for the pulse stretcher. A fiber Bragg grating is compact and suitable for moderate peak powers at the pre-amplification stages of a pulse stretcher. The cumulative group velocity dispersion of a properly designed fiber Bragg stretcher can be cancelled by a dispersion of opposite sign in the new compressor [20]. When the two are exactly balanced, ultra-short, clean, high peak power pulses can be produced at the output of the compressor.

With large dispersion angles and long effective optical lengths attainable, this design is capable of significantly reducing the compressor size by minimizing both the longitudinal and transverse dimensions of the compressor. By integrating optical components into a fused silica base material, this design is both robust and compact. In the next chapter, we will theoretically calculate how much influence this structure can have on a compressor system.

3. Compressor volume computation

It is not generally obvious that the compressor volume can be calculated using simple ray-tracing or the Taylor series expansion method. Here, we use the common Treacy compressor to illustrate both methodologies in Section 3.1 and 3.2, respectively. For simplicity, consider only the volume enclosed by the two gratings since this constitutes the main body of the compressor. Furthermore, assume that the grating width is linearly dependent on the grating separation distance, L, making this the important parameter to determine. The results obtained from these two methods are compared and analyzed. It turns out that both methods give the same results regarding L, and thus they are both capable of computing conventional two-grating compressor volume. In Section 3.3, we first investigate the details of the trajectory of the optical beam for the pulse before determining the method for computing the volume of our novel monolithic compressor. For simplicity, a two-fold structure for the compressor is used as an example. The discontinuity in optical path addition makes it obvious that ray-tracing is the most suitable method to apply here. The equations for computing the volume of the designed monolithic compressor are then derived, and the results obtained from this set of equations are compared to those of traditional compressors. The compactness of the new monolithic compressor is proved theoretically.

3.1 The Taylor series expansion method

The compressor volume is closely related to the compression ratio, or in other words, the group delay experienced by wavelength components of the pulses over the entire compressor system. When the group delay difference experienced by the longest and shortest wavelength components in the pulse gets larger, the total volume of compressor gets correspondingly larger. Thus determining a relationship between group delay and compressor size will be the primary goal of this Section.

We start this derivation by expressing the phase delay $\emptyset(\omega) = n\omega x/c$ near the central frequency ω_0 of the pulse, because the first derivative of $\emptyset$ with respect to ω gives the group delay τ. Here n is the refractive index of material between the two gratings that compose the compressor. In most situations, compressors are built in free space, so n equals 1, and x is the effective optical path traveled by an arbitrary frequency component ω, while c stands for the velocity of light throughout this derivation. Since the phase delay introduced by the grating pair varies slowly with frequency over the bandwidth of the incident pulse, it can be expressed in a form of a Taylor series [31] around a central pulse frequency ω_0. In most systems, it is enough to expand the series as far as the third order term, in which case:

$$\phi(\omega) = \phi_0 + a_1(\omega - \omega_0) + \frac{1}{8}a_2^2(\omega - \omega_0)^2 + \frac{1}{3}a_3^3(\omega - \omega_0)^3 ... \qquad \textbf{(3.1)}$$

where

$$a_1 = \frac{d}{d\omega}\left(\frac{n\omega x}{c}\right)\bigg|_{\omega_0}, \qquad \textbf{(3.2)}$$

$$a_2^2 = 4\frac{d^2}{d\omega^2}\left(\frac{n\omega x}{c}\right)\bigg|_{\omega_0}, \qquad \textbf{(3.3)}$$

$$a_3^3 = \frac{1}{2}\frac{d^3}{d\omega^3}\left(\frac{n\omega x}{c}\right)\bigg|_{\omega_0}. \qquad \textbf{(3.4)}$$

Now we can start from this general equation that applies to any common two-grating compressors, and use it to explore the exact expression of τ for a specific compressor set-up. The key parameter that needs to be found is the optical path x. Then the explicit form of equations 3.2-3.4 can be obtained. Based on this, τ, the first derivative of $\emptyset$ with respect of ω, can also be extracted. Note that while parameters selections may be different for various derivations, the core physics behind them are the same for all conventional two-grating compressors.

To better appreciate the physics behind equation 3.1, we will apply it to a real compressor. Consider a canonical compressor system to be comprised of two transmission gratings as shown in Figure 3.1. They are mounted with their faces parallel to each other. The two solid bold lines labeled G represent the grating planes, while the solid blue lines represent the beam trajectory. The distances AC and CB are equal; the line CD is parallel to and in the same direction as the incident beam; BD is perpendicular to CD. The perpendicular distance between the planes where the gratings are is L. The input angle is θ and the output angle of arbitrary order m is γ. The grating constant (period) is d.

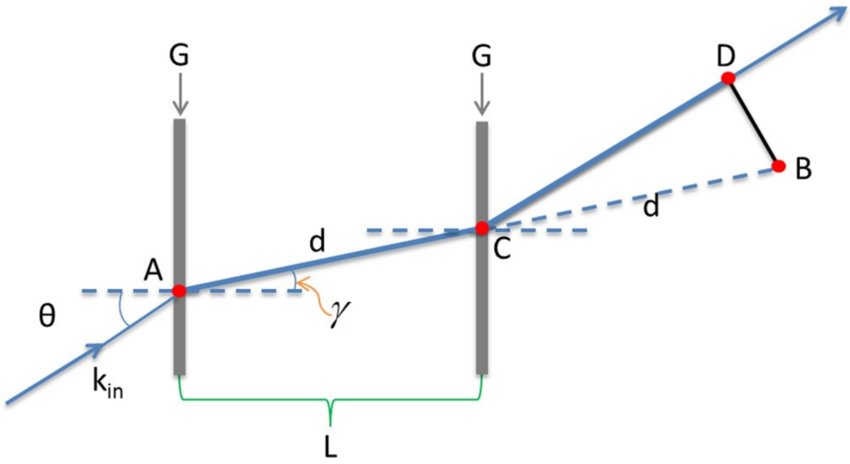

Figure 3.1 A canonical Treacy compressor comprised of two transmission gratings.

The effective optical path, P, traversed by an arbitrary frequency component, ω, between the point of incidence A and the equivalent image point B is given by:

$$\mathrm{P} = \frac{L\left[1+\cos\left(\theta-\gamma\right)\right]}{\cos\left(\gamma\right)} \quad \textbf{(3.5)}$$

Note that P is a function of ω.

Each frequency component propagates a unique distance P and thus is delayed in a phase by:

$$\phi(\omega) = \frac{\omega}{c}\mathrm{P} - \frac{2\pi L}{d}\tan\left(\gamma\right) \quad \textbf{(3.6)}$$

The grating equation which gives the frequency dependence of the diffracted angle is:

$$\sin(\theta) + \sin(\gamma) = \frac{2\pi c m}{\omega d} \quad \textbf{(3.7)}$$

where ω corresponds to an arbitrary frequency; d is the grating constant, and m is the diffraction order.

From equations (3.5, 3.6, 3.7), we can derive the expansion coefficients (3.2, 3.3, 3.4) for phase delay as:

$$a_1 = \frac{L\left[1+\cos(\theta-\gamma)\right]}{c\cos(\gamma)} \tag{3.8}$$

$$a_2^2 = \frac{-4L}{c\omega_0\cos(\gamma)}\left(\frac{m2\pi c}{\omega_0 d}\right)^2 \tag{3.9}$$

$$a_3^3 = \frac{3L}{2c\omega_0^2\cos^5(\gamma)}\left(\frac{m2\pi c}{\omega_0 d}\right)^2\left[\cos^2(\gamma)+\left(\frac{m2\pi c}{\omega_0 d}\right)\sin(\gamma)\right] \tag{3.10}$$

Since group delay is $\tau = \partial\emptyset/\partial\omega$, by substituting these coefficients into equation 3.1 and taking the derivative will give us the group delay. Using expressions 3.5 and 3.7 in the expression for the group delay for an arbitrary wavelength $\lambda = \lambda_0 + \delta\lambda$ for a double pass in the compressor results in

$$\tau = \frac{4L}{c\cdot\cos\theta} + \frac{2m^2L\lambda_0\delta\lambda}{cd^2\cos^3\gamma} + \frac{3m^2L\left(\delta\lambda\right)^2}{cd^2}\left(\frac{1}{\cos^3\gamma} + \frac{m\lambda_0\sin\gamma}{d\cos^5\gamma}\right), \tag{3.11}$$

where λ_0 is the central wavelength; L is the separation between the gratings; m is the diffraction order; d is the grating constant.

This equation gives the relationship between group delay and grating separation L. Since L is directly related to compressor volume, the relationship between compressor volume and group delay has thus been determined. So the next task is to use the group delay as an intermediate variable, and convert this equation to finding the relationship between the compressor volume and the grating constant. The grating size W can be obtained simply from the product of the grating separation L and diffraction angle, so the relationship between the compressor volume V and grating constant d can therefore be obtained.

It is now possible to calculate the group delay difference between the longest and shortest wavelength components of a stretched pulse after compression. Note that we also have the relationship

$$T_{final} = T_{initial} - \tau_{\max} + \tau_{\min}, \qquad \textbf{(3.12)}$$

where T_{final} is the final pulse width, and $T_{initial}$ is the initial pulse width. Since the initial pulse width minus the group delay difference between the longest and shortest wavelength components gives us the final pulse width, these parameters can be treated as known values of the system. Furthermore, we take $m = -1$ since it is the first diffraction order that has the most energy. From equation 3.11, we note that there are still four unknown parameters: θ, L, d, and Υ.

To reduce the number of unknown parameters, we use the Littrow condition to calculate the appropriate angle of incidence for the beam. According to the Littrow condition, if we want to have the most energy in a certain diffracted order, we should have the incident angle equal to the diffracted angle. Thus if we apply the Littrow condition to the central wavelength component and designate that the majority of the energy is refracted to the first order, the input angle can be simply expressed by:

$$\theta = \arcsin\left(\frac{\lambda_0}{2d}\right) \qquad \textbf{(3.13)}$$

Thus the angle of incidence θ is determined by the grating constant. According to the grating equation 3.7, the diffracted angle also depends on the grating constant. The only remaining unknown parameters are L and d.

The spectral bandwidth of the pulse is $\delta\lambda$; the maximum and minimum group delays, τ_{max} and τ_{min}, are specified by the boundary wavelength conditions where $\lambda = \lambda_0 \pm \delta\lambda/2$. This means the corresponding diffraction angles Υ_{max} and Υ_{min} can be calculated using the grating equation 3.7. Consolidating this information in

3.12, one can solve for the $L-d$ relationship and arrive at the expression

$$L=\left(T_{initial}-T_{final}\right)\cdot\left\{\begin{array}{l}\left[\dfrac{m^2\lambda_0\Delta\lambda}{cd^2\cos^3\gamma_{\max}}+\dfrac{3m^2\left(\Delta\lambda\right)^2}{4cd^2}\left(\dfrac{1}{\cos^3\gamma_{\max}}+\dfrac{m\lambda_0\sin\gamma_{\max}}{d\cos^5\gamma_{\max}}\right)\right]\\-\left[\dfrac{-m^2\lambda_0\Delta\lambda}{cd^2\cos^3\gamma_{\min}}+\dfrac{3m^2\left(\Delta\lambda\right)^2}{4cd^2}\left(\dfrac{1}{\cos^3\gamma_{\min}}+\dfrac{m\lambda_0\sin\gamma_{\min}}{d\cos^5\gamma_{\min}}\right)\right]\end{array}\right\}^{-1}, \quad \textbf{(3.14)}$$

with

$$\gamma_{\max}=\arcsin\left(\frac{\lambda+\Delta\lambda/2}{d}-\sin\theta\right), \quad \textbf{(3.15)}$$

$$\gamma_{\min}=\arcsin\left(\frac{\lambda-\Delta\lambda/2}{d}-\sin\theta\right). \quad \textbf{(3.16)}$$

As stated earlier, the grating size W is linearly dependent on the grating separation L as:

$$W=L\cdot(\gamma_{\max}-\gamma_{\min}). \quad \textbf{(3.17)}$$

The W gives the width of grating in the direction that is perpendicular to its rulings. In the direction that is parallel to the rulings, the grating height H is set to be a same fixed value that applies to all the calculations regarding both traditional and novel monolithic compressors throughout this discussion. Since there are no feature changes in this direction, it only needs to be chosen a reasonable value that is larger than the input beam spot size. Thus the compressor volume can be expressed as $V=L\times W\times H$. However, as mentioned before, because H is the same for all calculations, and W is linearly dependent on L, we will only need to focus our discussion on $L-d$ relationship. This relationship contains all the information we need for computing the compressor volume.

3.2 Ray-tracing method

The grating volume can also be calculated using the ray tracing method. We are, as stated in the last Section, initially interested in the group delay experienced by different wavelength components. We then will use the group delay as an intermediate variable for finding the relationship between the compressor volume V and the grating constant d. Again, since the compressor volume is linearly dependent on the separation between the gratings, L, we will focus our primary discussion on finding the $L-d$ relationship. The trajectories taken of the diffracted beam are as shown in Figure 3.2.

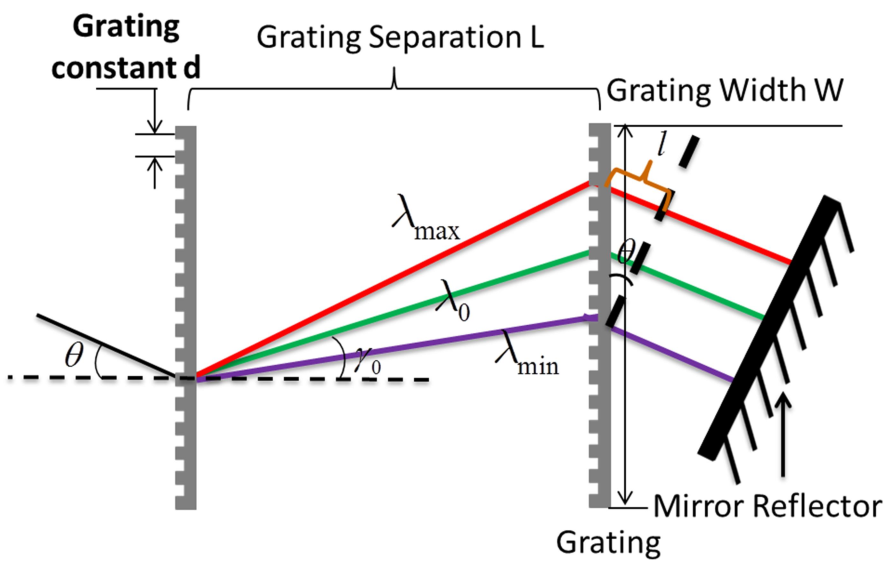

Figure 3.2 Diffracted beam trajectories in traditional Treacy compressor.

Upon hitting the first grating, different wavelength components get angularly spread out. According to the grating equation, one can express the angle of diffraction in terms of the angle of incidence. The angle of incidence, in turn, can be obtained from the Littrow condition. In order to have most energy in the first-order diffracted beam, the angle of incidence must be equal to the diffracted angle, which is the Littrow condition. We apply this condition to the central wavelength component and take it that the majority of the energy is diffracted to the first order. Applying this condition to the central wavelength λ_0, and using the grating equation 3.7 and the Littrow condition 3.13 yields

$$\gamma = \arcsin\left(\frac{\lambda}{d} - \frac{\lambda_0}{2d}\right). \quad \textbf{(3.18)}$$

The angle of incidence, θ, is shown as in Figure 3.2 with respect to the normal to the grating surface. The longest wavelength component will be diffracted at an angle larger than Υ_0, and similarly, the shortest wavelength component will be diffracted at an angle smaller than Υ_0; we call these angles Υ_{max} and Υ_{min}, respectively. They naturally follow the grating equation, and can be expressed as

$$\gamma_{\max} = \arcsin\left(\frac{\lambda_{\max}}{d} - \frac{\lambda_0}{2d}\right); \quad \textbf{(3.19)}$$

$$\gamma_{\min} = \arcsin\left(\frac{\lambda_{\min}}{d} - \frac{\lambda_0}{2d}\right). \quad \textbf{(3.20)}$$

We now calculate the time delay between the longest and shortest wavelength components. First, we calculate the delay between the two gratings. Since the separation between them is L, the time delay within the gratings is

$$\tau_{left} = \frac{\left(\dfrac{L}{\cos\theta_{\max}} - \dfrac{L}{\cos\theta_{\min}}\right)}{c}. \quad \textbf{(3.21)}$$

The second interval of the delay is between the second grating and the mirror reflector. Upon exiting the second grating, the diffracted wavelength components follow the trajectories indicated in Figure 3.2; note that by geometric congruence the line that intersects the diffracted beams perpendicularly (shown in dashed form) subtends an angle θ with the back surface of the second grating. So the distance l, which depends on the path of a particular wavelength, can be calculated in terms of the angle θ. Therefore the difference between the distance for the longest and shortest wavelength components can derived as

$$L(\tan\gamma_{\max} - \tan\gamma_{\min})\sin\theta. \quad \textbf{(3.22)}$$

If the initial pulse width is designated as τ_0, after one round trip through the compressor system, the final pulse width will be:

$$\tau = \tau_0 - \frac{2}{c}\left\{\left[\frac{L}{\cos\gamma_{\max}} + L\left(\tan\gamma_{\max} - \tan\gamma_{\min}\right)\sin\theta\right] - \frac{L}{\cos\gamma_{\min}}\right\}. \quad \textbf{(3.23)}$$

After rearranging the terms, one obtains the $L-d$ relationship as:

$$L = \frac{c\left(\tau_0 - \tau\right)}{2}\left\{\left[\frac{1}{\cos\gamma_{\max}} + \left(\tan\gamma_{\max} - \tan\gamma_{\min}\right)\sin\theta\right] - \frac{1}{\cos\gamma_{\min}}\right\}^{-1}, \quad \textbf{(3.24)}$$

with θ given by Littrow condition 3.13, and $\Upsilon_{\max}$ and $\Upsilon_{\min}$ given by equation 3.15 and 3.16, respectively.

For the sake of a concrete example, we take the central wavelength of a pulse to be at 1030 nm, with a spectral bandwidth of 80 nm. Also, let the initial pulse width (after stretching from 1 ps) be 1 ns; the final compressed pulse width should be equal to 1 ps. Using these parameters, the plots of the $L-d$ relationships obtained by the two different methods are shown in Figure 3.3.

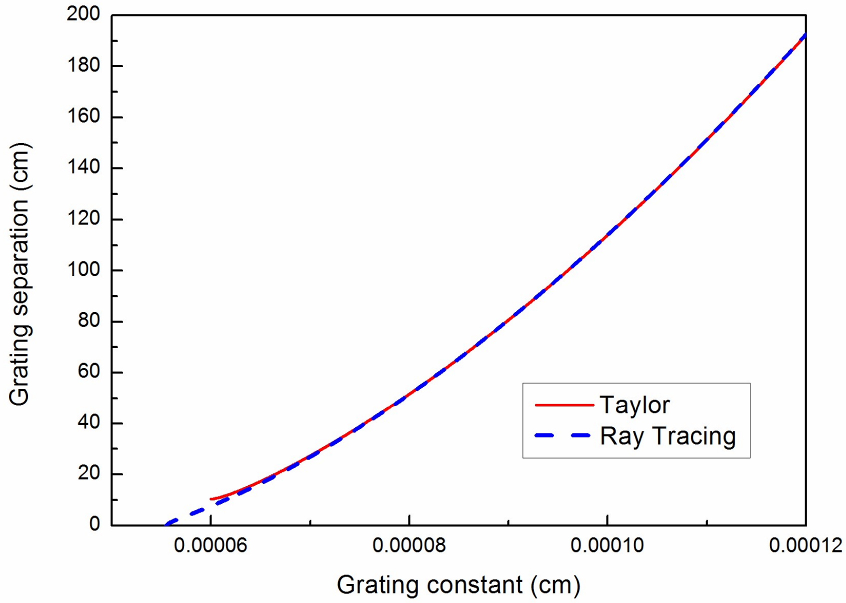

Figure 3.3 The L-d relationship for a compressor as determined by ray-tracing and Taylor series analyses methods.

The results obtained by the two methods overlap when the grating constant is relatively large. However, they disagree dramatically when the grating constant is or smaller than 600 nm. This can be attributed to the fact that higher order terms of the Taylor series expansion are discarded in the analysis. One should also note that ray-tracing is valid for objects whose dimensions are larger than the wavelength of light in question. This implies that any results obtained for grating constants smaller than the light wavelength, may be questionable. The general conclusion, however, is that the two methods can be used to estimate compressor size. The observed trend indicates that compressor size decreases as grating ruling gets denser.

3.3 Volume of new compressor

3.3.1 Calculation methodology evaluation

Although either the Taylor series expansion method or the ray-tracing method can be used to estimate the size of a conventional compressor, we will not use the Taylor series expansion method to estimate the size of the proposed monolithic compressor. The Taylor series expansion method requires that group delay should change slowly and smoothly with frequency. In the new compressor, the optical paths of the constituent wavelengths can have sudden changes, and as a consequence, the group delay can be discontinuous. The best approach therefore for estimating the size of the new compressor is ray-tracing.

The new volume calculation involves finding the trajectory of every wavelength component in two regions: the space between the two gratings, and the space between the second grating and the integrated rear mirrors. Since folding the optical path of the beam does not change the physics relative to the traditional two-grating compressor, the path traveled by each wavelength component between the two gratings will not change in the new compressor. The changes in the optical path are between the second grating and the integrated reflecting back mirror. In the conventional compressor, the longest wavelength component travels the longest distance between the second grating and the back mirror. For the new design, there is an additional sawtooth-like distance after the second grating. We will demonstrate in the following section how this change comes about.

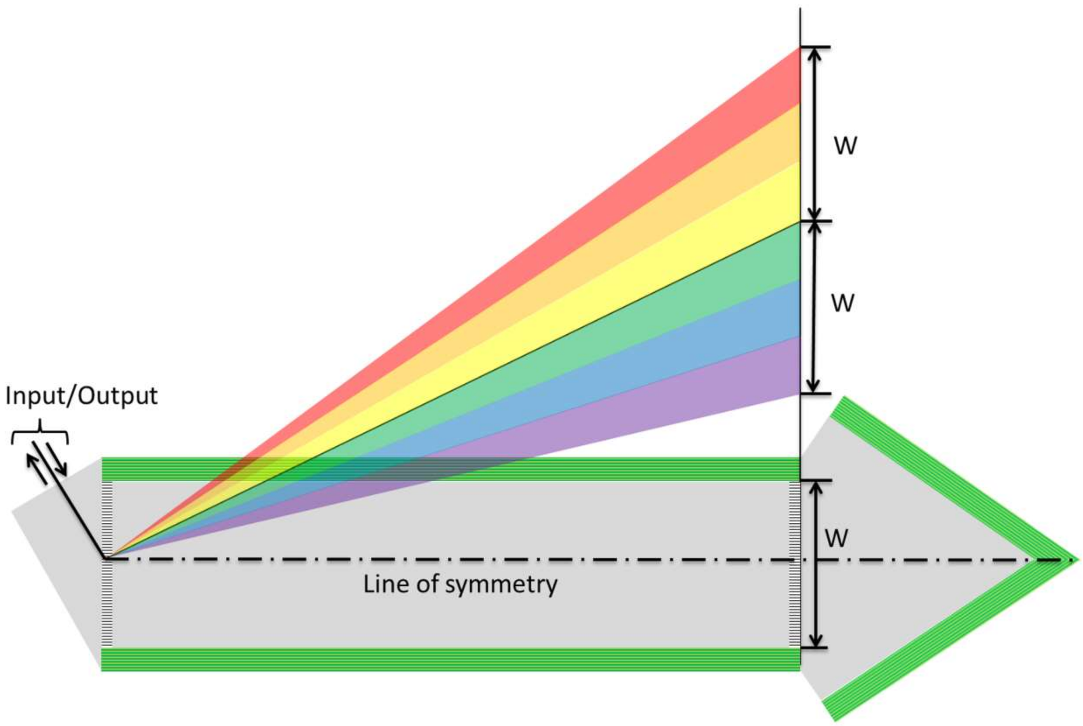

Figure 3.4 Beam trajectory in the compressor without a folding mechanism.

Although the optical path difference and beam physics do not change in between the two gratings, the optical field here is consistent with that in the space between the second grating and the integrated rear mirrors. Therefore we will start our discussion with investigation of the field in this space.

As illustrated in Figure 3.4, different wavelength components get angularly spread out after exiting the first grating of the compressor. In the absence of folding surfaces at the edges of the block (as it is the case in the conventional two-grating compressors), the different colors would fan out to form a triangle as indicated. A large second grating would re-collimate the beam and fix the group delay to a certain value. In the conventional compressor, every wavelength component has a unique point of intersection with the second grating.

However, with the beam-folding reflecting surfaces in place at the edges of Block

2, the diffracted and folded wavelength components still ultimately reach the second grating and intersect with it. Wavelength components separated by a distance that is an integer multiple of times of the grating width W (indicated in Figure 3.4) will share the same point of intersection at the second grating.

For this reason, it is convenient to choose the compressor parameters such that the divergence of the spread of wavelengths is exactly an integer multiple of times of the grating width. For simplicity, we show in Figure 3.4 a case where the wavelength spread is twice as large as the grating width. This way, the beam after the first grating is divided into two components.

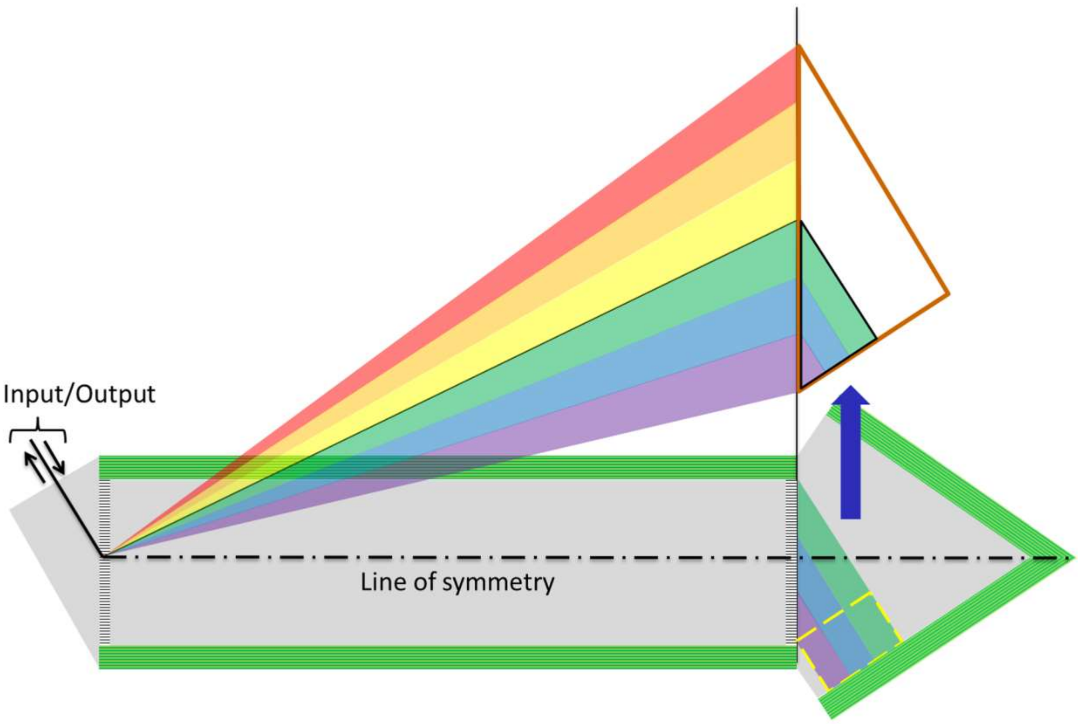

Figure 3.5 Optical path length in Block 3 for the shorter wavelength band of diffracted light.

When the initial input point to the compressor system is adjusted such that the two components of light in Figure 3.4 fully intersect the second grating, the beam trace for the shorter band of wavelengths (the lower triangle) will propagate toward Block 3 as shown in Figure 3.5. It forms a violet-colored trapezoid inside Block 3 with two of its sides perpendicular to the rear mirror, and one side overlaps with the mirror surface. Note that this illustration assumes the lower band is reflected for an even number of times by the side coatings. It can also be reflected for an odd number of times, which does not make a difference in the optical path difference in block 3, because the compressor is symmetric about the horizontal central line indicated with the dashed black line.

Without a beam folding structure, this would become identical to what happens in a traditional grating compressor. The additional optical path length after the second grating for the total of these two portions would be the large triangular area outlined by the solid brown lines (in the upper right corner of Figure 3.5). The vertical distance, from the intersection point for each wavelength component on the second grating to the side of triangle that is parallel to the lower rear mirror, represents the optical path addition of corresponding wavelength component. As can be seen, longer wavelength components get larger optical path additions, while shorter wavelength components get smaller optical path additions.

In contrast to the traditional compressor, the monolithic compressor has each of the divided component bands retro-reflected separately. Assuming that the shorter wavelength band (in the lower portion) of the light in Block 2 is reflected by an even multiple of times by the reflective folding surfaces, the second grating will diffract it to a direction that is parallel to the original light input direction to the system; this is illustrated as shown in Block 3 of Figure 3.5.

Since what matters is the difference between the additional optical paths for the different wavelength components, the path-lengths in the square enclosed by the yellow dashed lines will not be considered. The effective additional optical path lengths for the shorter wavelength band (of the lower portion) are therefore represented by the violet-colored triangular region that is located in the upper right corner.

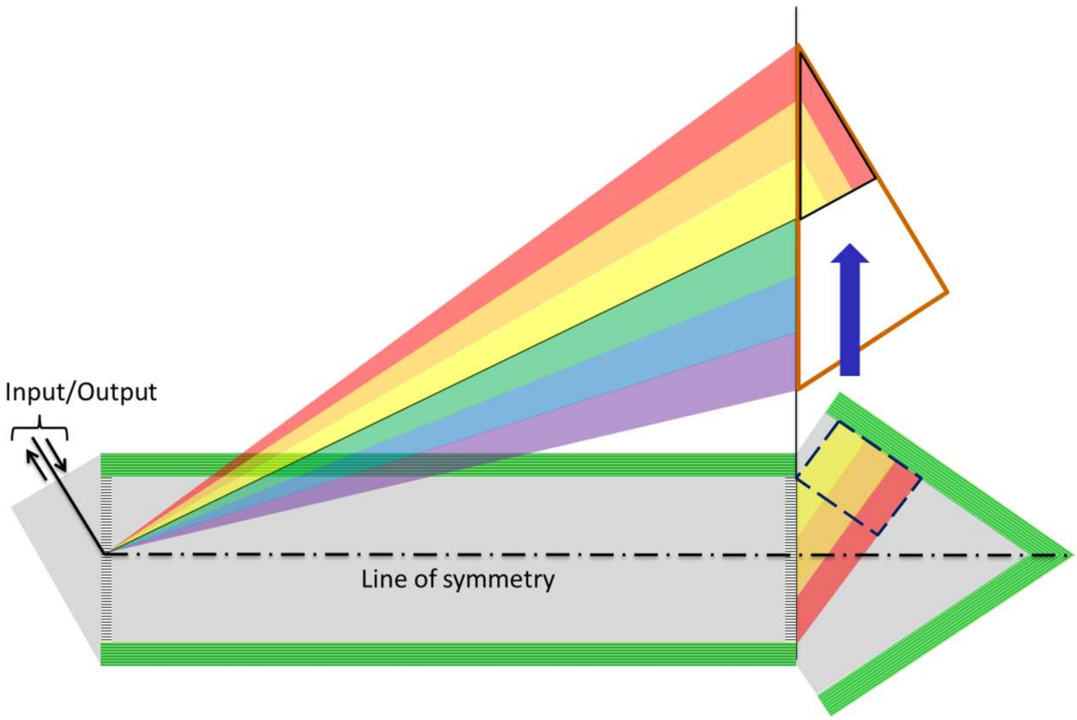

Figure 3.6 Beam trajectory in Block 3 for longer wavelength band of diffracted light.

Now consider the portion of light that constitutes the longer band of wavelengths. This band (illustrated in the upper portion of Figure 3.6) of the diffracted light will be folded by an odd multiple of times, which is consistent with the former discussion on the lower band. After exiting the second grating, this band will propagate along a direction that has a mirror reflection symmetry to the original input light; the line of symmetry is the system axis (indicated by the dashed black line). The band area inside

Block 3 is indicated in Figure 3.6. As before, the optical path difference enclosed in the square with blue dashed lines will not be considered. The effective additional optical path length for the band is represented by the triangular area enclosed by solid black lines (in the upper right-hand portion) of Figure 3.6.

The discontinuities in the optical path lengths described above represent additional optical path lengths in Block 3 as indicated by the little triangles (in the upper right-hand portion) of Figure 3.7. In the illustrative example discussed above, partition of the wavelength components into two bands results in two little triangles; if the wavelength components are partitioned into multiple bands, then correspondingly more little triangles will be generated, resulting in what looks like a saw-tooth structure. Because of this discontinuity, the Taylor series expansion method is not applicable here, and the volume of this monolithic compressor should be derived following the ray tracing method.

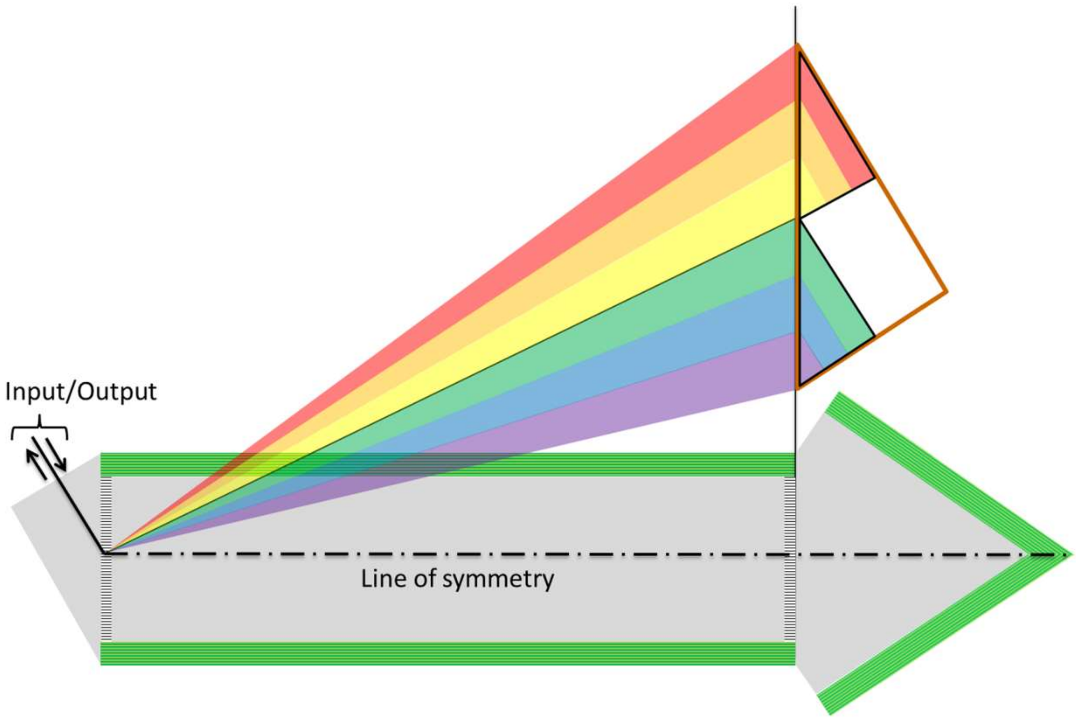

Figure 3.7 Addition of saw-tooth-like path lengths in Block 3.

3.3.2 Comparison of the calculations of compressor volume

The total effective optical path length for a given central wavelength is simply the sum of the path lengths between the two gratings and the additional path length contributed by the little triangular region after the light exits the second grating. To illustrate, assume that the original input light point to the system is at the center of the input surface; the total path length for an arbitrary central wavelength will be as indicated by the black lines in Figure 3.8.

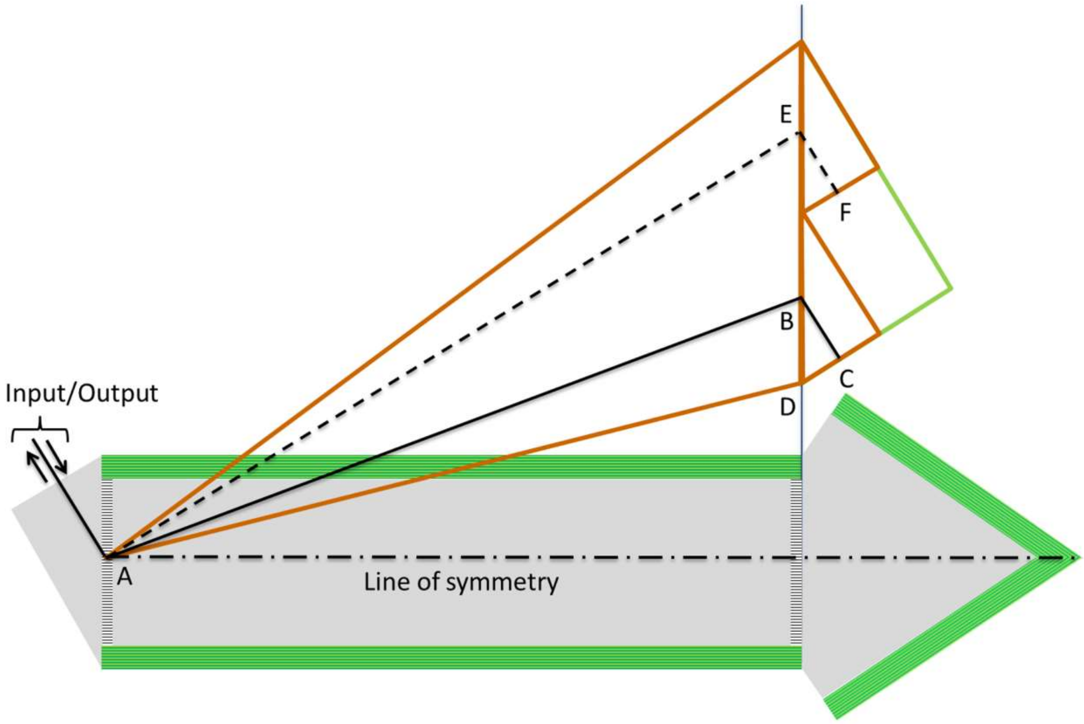

Figure 3.8 Beam trajectory for an arbitrary central wavelength.

If this wavelength component falls in the shorter wavelength band, the path length is given by the sum of AB and BC. The path length BC can be obtained by referencing the expression for BD, and in turn, BD and AB is directly related to L. According to the principles of ray-tracing, the optical path length traveled by an arbitrary wavelength component for the shorter wavelength band is given by

$$P = \frac{nL}{\cos\gamma_\lambda} + n\left[L\tan\gamma_\lambda - L\tan\gamma_{\min}\right]\sin\theta, \qquad \textbf{(3.25)}$$

where Υ_λ is the diffraction angle of the arbitrary wavelength in question, n is the refractive index of the compressor material, L is the separation between the gratings, $\Upsilon_{\min}$ is the diffraction angle of the shortest wavelength component, and θ is the input angle.

For additional light bands beyond the shorter wavelength ones, the optical path lengths AE and EF need to be scaled by W, the width of the grating. Thus the effective path length is given by

$$P = \frac{nL}{\cos\gamma_\lambda} + n\left[L\tan\gamma_\lambda - L\tan\gamma_{\min} - M\cdot W\right]\sin\theta, \tag{3.26}$$

where M is an integer. Note that

$$0 \le L\tan\gamma_\lambda - L\tan\gamma_{\min} - M\cdot W \le W. \tag{3.27}$$

The shortest possible optical path length for the shortest wavelength is therefore

$$P = \frac{nL}{\cos\gamma_\lambda}. \tag{3.28}$$

And for the longest wavelength, it is

$$P = \frac{nL}{\cos\gamma_\lambda} + nW\sin\theta. \tag{3.29}$$

For the compressor to function properly, two restrictions must be imposed. The first is connected to pulse compression physics; the group delay of the longest and shortest wavelength components must be sufficient to allow pulse compression to the shorted possible pulse. The second restriction relates to compressor geometry; the beam divergence should be an integer multiple of times of the grating width. There are therefore two simultaneous equations that must be solved for the grating width, W, and the grating separation, L. These equations are:

$$\frac{nL}{\cos\gamma_{\max}} + nW\sin\theta - \left(\frac{nL}{\cos\gamma_{\min}}\right) = \frac{c}{2}\left(T_{final} - T_{initial}\right), \tag{3.30}$$

$$L\tan\gamma_{\max} - L\tan\gamma_{\min} = N\cdot W, \tag{3.31}$$

where $\Upsilon_{\max}$ is the diffraction angle of the longest wavelength component; c is the velocity of light, T_{final} is the final pulse width, and T_{initial} is the initial pulse width.

The variable N is an integer that is different from the previous integer, M.

As an illustrative calculation, assume that the central wavelength for a given pulse train is 1030 nm, with a spectral bandwidth of $\Delta\lambda = 80$ nm; the grating parameter will be taken to be $d = 600$ nm. Furthermore, assume that a typical grating has a height of 40 mm. This is reasonable since input light into a compressor in the vertical plane has no special feature. The calculated parameter results for the traditional and new monolithic compressors are listed in Table 3.1.

Table 3.1 Comparison of compressor parameters in moderate condition.

Pulse parameters		
Input pulse width	1 ns	
Output pulse width	1 ps	
Compressor parameters		
	Common compressor	Monolithic compressor
Number of divisions M	0	2
Grating separation L	7.60 cm	6.97 cm
Grating width W	7.60 cm	3.97 cm
Grating Height H	4 cm	4 cm
Compressor volume	231.04 cm^3	110.68 cm^3

Evidently the new compressor occupies less than half the volume of a conventional compressor for the same parameter values. This holds for when the beam divergence is twice as wide as the grating width. If this is larger, the compressor volume will be further reduced. For example, for the extreme case where pulses are compressed from 3 ns to 500 fs, with a bandwidth of 300 nm, and a grating parameter d of 700 nm, and where the wavelength components are partitioned into 6 bands, the conventional compressor volume would be as large as 1349.52 cm^3, while the new compressor would only be 287.71 cm^3 (Table 3.2).

Table 3.2 Comparison of compressor parameters in severe condition.

Pulse parameters		
Input pulse width	3 ns	
Output pulse width	500 fs	
Compressor parameters		
	Common compressor	Monolithic compressor
Number of divisions M	0	6
Grating separation L	11.78 cm	13.32 cm
Grating width W	28.64 cm	5.40 cm
Grating Height H	4 cm	4 cm
Compressor volume	1349.52 cm^3	287.71 cm^3

4. Pulse compression simulation

The response of the new monolithic compressor to a single chirped Gaussian pulse is numerically simulated utilizing the finite-difference time-domain (FDTD) method. In section 4.1, a brief review of the FDTD algorithm and implementation are first given, using a one-dimensional example for the simulation. Then in Section 4.2, a two-dimensional simulation grid defining the monolithic compressor structure is described. Implementation details of the oblique chirped source, two kinds of reflectors, and the blazed grating structure are also given. With all essential optical elements collected, we present in Section 4.3, the parameters and corresponding results obtained from the simulation of the monolithic pulse compressor. First, the simulation grid is properly discretized, and then the input source parameters are adjusted accordingly to provide the right amount of dispersion. The electric field plots obtained from the simulation validate our previous discussion on the beam propagation traces inside monolithic compressor. The recorded electric field pulse amplitude and intensity prove the existence of the saw-teeth like optical path addition in the monolithic compressor. When the monolithic compressor is paired with a properly designed fiber Bragg grating, clean ultra-short and high-peak-power laser pulses can be produced. Possible improvements of the compressed pulse are proposed in Section 4.4.

4.1 Brief review of FDTD method

Maxwell's equations give the dependency of electric and magnetic fields on each other, and their propagation through space at a velocity *c*, which happens to be the velocity of light. The time evolution of fluctuating electric and magnetic fields is coupled. This is the fundamental theory that the finite-difference time-domain (FDTD) method is based on. The FDTD method employs finite differences as approximations to both the spatial and temporal derivatives that appear in Maxwell's equations (specifically Ampere's and Faraday's laws), and solves for future unknown fields based on the past known fields.

The FDTD algorithm was first proposed by Kane Yee in 1966 [32]. The algorithm can be summarized as follows [33]:

1. Rewrite all the derivatives in Ampere's and Faraday's laws in discretized form. The electric and magnetic fields should be staggered in both space and time. Solve the resulting difference equations to obtain "update equations" that express the (unknown) future fields in terms of (known) past fields.

2. Move one time-step into the future and solve for the magnetic fields, and then move another time-step into the future and solve for the electric fields.

3. Repeat the previous step until a proper time step is reached, and desired fields have been obtained.

To demonstrate the methodology, and for simplicity, we take a 1D electro-magnetic field FDTD simulation as an example. In the 1D case, assume we have source-free space where there are only variations in the x direction, and the electric field only has a z component. Faraday's law and Ampere's law can be written as:

$$-\mu\frac{\partial H}{\partial t}=\nabla\times E=\begin{vmatrix} a_x & a_y & a_z \\ \frac{\partial}{\partial x} & 0 & 0 \\ 0 & 0 & E_z \end{vmatrix}=-a_y\frac{\partial E_z}{\partial x}\rightarrow\mu\frac{\partial H_y}{\partial t}=\frac{\partial E_z}{\partial x}, \quad \textbf{(4.1)}$$

$$\varepsilon\frac{\partial E}{\partial t}=\nabla\times H=\begin{vmatrix} a_x & a_y & a_z \\ \frac{\partial}{\partial x} & 0 & 0 \\ 0 & H_y & 0 \end{vmatrix}=a_z\frac{\partial H_y}{\partial x}\rightarrow\varepsilon\frac{\partial E_z}{\partial t}=\frac{\partial H_y}{\partial x}. \quad \textbf{(4.2)}$$

Here μ is permeability; H is magnetic field; ε is permittivity; and E is electric field. a_x, a_y, and a_z are the unit vectors in x, y, z directions, respectively.

As will be shown, the first equation will be used to advance the magnetic field in time while the second will be used to advance the electric field. A method in which one field is advanced and then the other, and the process is repeated, is known as a leap-frog method. The next step is to replace the derivatives in equation 4.1 and 4.2 with finite differences. A second order central-difference approximation is used to represent differential fields at discretized points.

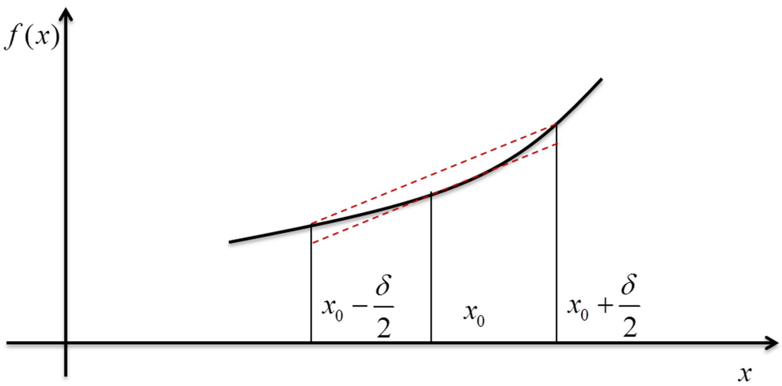

Figure 4.1 Central-difference approximation.

As illustrated in Figure 4.1, the central-difference approximation is given by:

$$\left.\frac{df(x)}{dx}\right|_{x=x_0} \approx \frac{f(x_0+\frac{\delta}{2})-f(x_0-\frac{\delta}{2})}{\delta}. \qquad \textbf{(4.3)}$$

This basically approximates the derivative at point x_0 based on neighboring sample points that are separated by a distance δ. The smaller δ is, the more accurate this approximation can be. In the limit as δ goes to zero, the approximation becomes exact.

To represent discretized electric and magnetic fields in space and time, the following notations are used:

$$E_z(x,t) = E_z(m\Delta x, q\Delta t) = E_z^q[m]; \qquad \textbf{(4.4)}$$

$$H_y(x,t) = H_y(m\Delta x, q\Delta t) = H_y^q[m]. \qquad \textbf{(4.5)}$$

Here Δx is the unit space step size, and Δt is the unit time step size. Correspondingly, m is the discretized spatial step, and q is the temporal step. In the following discussion, the last form is used to represent fields at point m at time step q. In FDTD simulations, the spatial indices are used explicitly as field array indices, while the temporal indices are specified and updated as global variables.

The nodes are arranged in space and time as show in Figure 4.2. Although we are dealing with one-dimensional problem, time can be treated as another dimension. So this can actually be thought of as a two-dimensional problem.

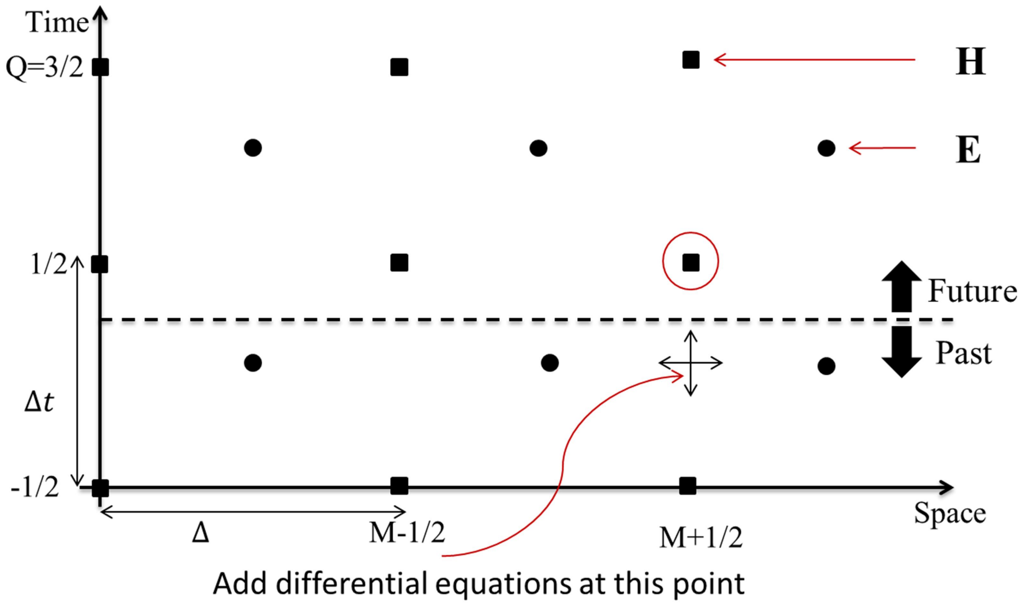

Figure 4.2 Electric- and magnetic-field sample points in space and time for magnetic field updating.

The electric-field nodes are shown as circles and the magnetic field nodes as squares. The dashed line represents the boundary between future and past time. So that all the fields below the dashed line are known, while the fields above the dashed line are unknown. The FDTD algorithm provides a way to obtain the future fields based on the past fields.

In order to solve for the unknown magnetic fields above the dashed line, we take the magnetic node circled in red as an example. The other nodes in the same line can be obtained in the same manner. As indicated in Figure 4.2, apply Faraday's law at the space-time point $((m + 1/2)\Delta x, q\Delta t)$, and we have:

$$\frac{\mu(H_y^{q+\frac{1}{2}}[m+\frac{1}{2}] - H_y^{q-\frac{1}{2}}[m+\frac{1}{2}])}{\Delta t} = \frac{E_z^q[m+1] - E_z^q[m]}{\Delta x} \tag{4.6}$$

Solve equation 4.6 for the future magnetic field, we have:

$$H_y^{q+\frac{1}{2}}[m+\frac{1}{2}] = H_y^{q-\frac{1}{2}}[m+\frac{1}{2}] + \frac{\Delta t}{\mu \Delta x}(E_z^q[m+1] - E_z^q[m]). \quad \textbf{(4.7)}$$

This is the update equation for magnetic field. It states that the future magnetic node value can be obtained if its past value and neighboring electric nodes are known. Referring to Figure 4.2, all the terms on the right side of equation 4.7 is underneath the dashed line that separate past and future. Thus all of these values are known values. If we apply equation 4.7 to all the magnetic nodes that have the same temporal step as the one we discussed, then all the magnetic field nodes at time step $q + 1/2$ can be obtained. The dashed line can therefore be moved one-half time step up, and we reach a situation as illustrated in Figure 4.3.

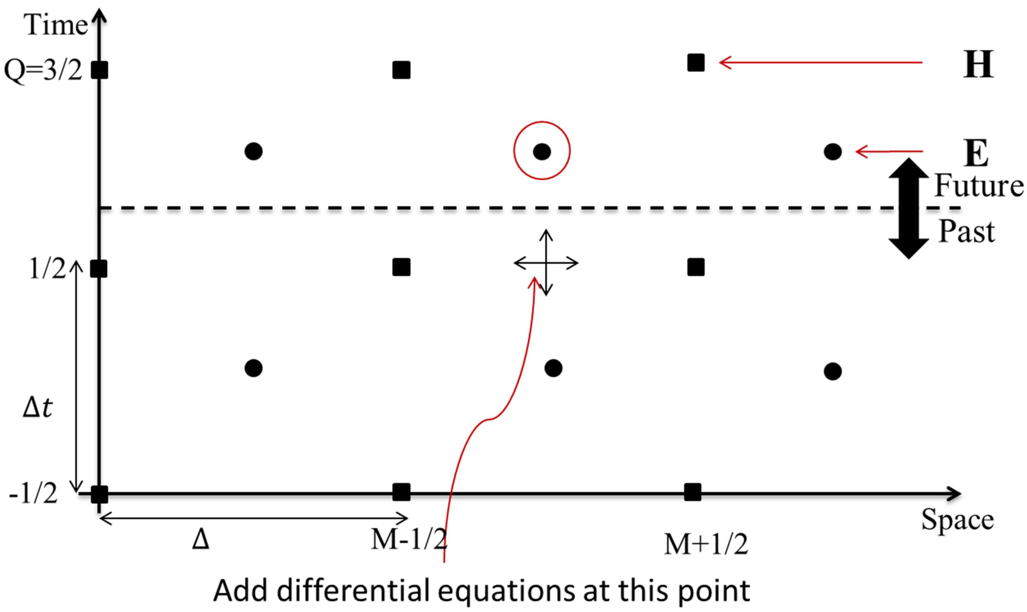

Figure 4.3 Electric- and magnetic-field sample points in space and time for electric field updating.

Again, to solve for the electric field nodes at time step $(q + 1/2)\Delta t$, which is positioned just above the past/future boundary line, we take the electric node circled in red as an example (Figure 4.3). Consider Ampere's law at the space-time point

$(m\Delta x, (q + 1/2)\Delta t)$ in a discretized form:

$$\varepsilon \frac{E_z^{q+1}[m] - E_z^q[m]}{\Delta t} = \frac{H_y^{q+\frac{1}{2}}[m+\frac{1}{2}] - H_y^{q+\frac{1}{2}}[m-\frac{1}{2}]}{\Delta x} \quad \textbf{(4.8)}$$

Solve equation 4.8 for the future electric field, we have:

$$E_z^{q+1}[m] = E_z^q[m] + \frac{\Delta t(H_y^{q+\frac{1}{2}}[m+\frac{1}{2}] - H_y^{q+\frac{1}{2}}[m-\frac{1}{2}])}{\varepsilon \Delta x} \quad \textbf{(4.9)}$$

Thus the future electric field is only dependent on its own past value and neighboring magnetic nodes. In the same manner as was done with the magnetic field, all the electric nodes at the same time step can be obtained, and the past/future boundary line can be moved one-half time step up. We then arrive at a situation where magnetic field nodes are the to-be-solved values again; this is exactly the same previous step. Repeated application of the two update equations for the magnetic and electric field nodes pushes the dividing line between past and future forward until the next designated time step is reached. The FDTD method is a convenient way of linking time and space in simulations in a way that allows future fields to be determined from past fields.

In FDTD simulations, spatial positions are represented with integer indices, and the electric and magnetic fields are discretized at many nodes that compose corresponding matrices. It appears in equation 4.7 and 4.9 that Δx and Δt should be explicitly specified in order to obtain updated values. However in a simulation, they can be replaced with a proportionality factor.

The ratio of how far energy can propagate in a single temporal step to spatial step,

$c\Delta t/\Delta x$, is often called the Courant number. It plays an important role in determining the stability of a simulation. From here on we will label it as S_c. The basic rule, which comes from the real world, states that an electro-magnetic field cannot propagate faster than the velocity of light. This in turn means the Courant number cannot be larger than $1/\sqrt{D}$, where D is the dimension of simulation. So in one-dimensional simulations, for example, S_c should be equal to or smaller than 1, which means the field propagates no more than one spatial step in one time step interval.

The coefficients that appear in the update equations 4.7 and 4.9 can now be represented with the Courant number as:

$$\frac{\Delta t}{\mu \Delta x} = \frac{1}{\mu_r \eta_0} S_c, \tag{4.10}$$

$$\frac{\Delta t}{\varepsilon \Delta x} = \frac{\eta_0}{\varepsilon_r} S_c. \tag{4.11}$$

Here $\eta_0 = \sqrt{\mu_0/\epsilon_0}$, and it is the characteristic impedance of free space. μ_r is relative permeability, and ϵ_r is relative permittivity.

Although this FDTD example of a simulation is in the one-dimensional case, the algorithm stays the same for FDTD simulations in higher dimensions. The electric and magnetic fields are discretized and staggered in space and time, and then update equations are applied to obtain future fields based on the past fields. Note that in FDTD simulations, all time and space variables are represented with time and spatial steps, respectively. The unit temporal step size should be small enough to discretize the shortest pulse, while the unit spatial step size should be chosen so that it is fine enough to resolve the wavelength of interest or the smallest feature size. These two factors are linked through the Courant number. Once one is chosen, the other is automatically fixed. The time and space variables can then be replaced with their corresponding multiples.

4.2 Compressor simulation system configuration

Apparently a simulation of the response of a monolithic compressor device to a pulse requires a higher dimension than one. Since there is no special feature that is changing in the direction that is parallel to the grating ruling in the pulse compression process [5], a plane that is perpendicular to the grating ruling will contain all the information that we need for pulse analysis, as long as it lies in the same horizontal level with the input and output pulse axes. Thus for this project, a two-dimensional FDTD simulation that works with a transverse magnetic field (TMz) is used to simulate the pulse response of the monolithic compressor.

TMz fields contain three field components: E_z, H_x, and H_y. Note that here the magnetic fields are transverse to the z direction. Assume the field is varying in both x and y directions, but not along the z direction. The three scalar equations that can be obtained from Faraday's and Ampere's law are:

$$-\sigma_m H_x - \mu \frac{\partial H_x}{\partial t} = \frac{\partial E_z}{\partial y} \tag{4.12}$$

$$\sigma_m H_y + \mu \frac{\partial H_y}{\partial t} = \frac{\partial E_z}{\partial x} \tag{4.13}$$

$$\sigma E_z + \varepsilon \frac{\partial E_z}{\partial t} = \frac{\partial H_y}{\partial x} - \frac{\partial H_x}{\partial y} \tag{4.14}$$

Here ϵ is the electrical permittivity, μ is the magnetic permeability, σ is the electric conductivity, and σ_m is the magnetic conductivity.

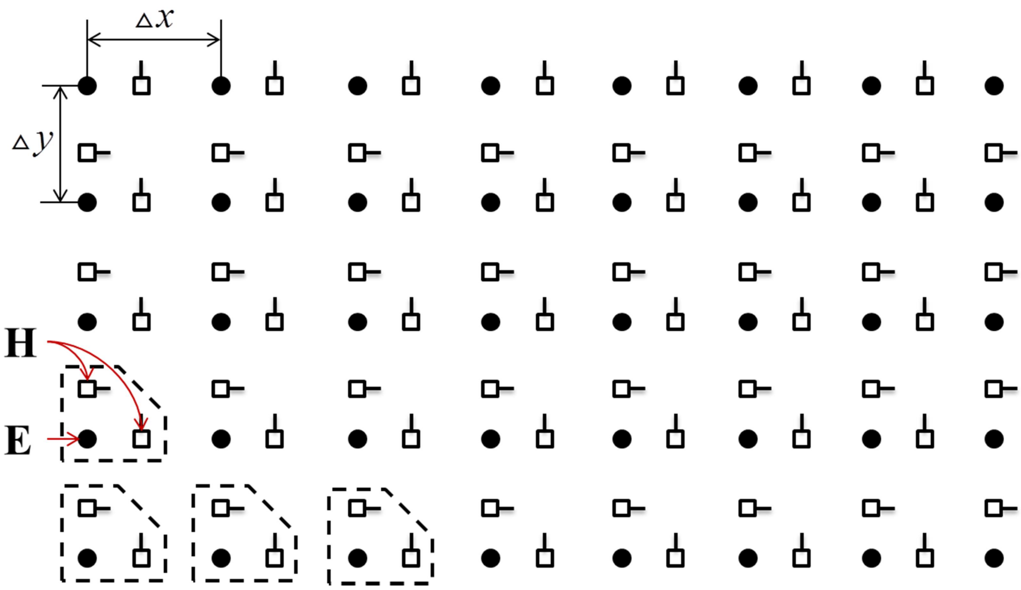

Figure 4.4 Electric and magnetic field sample points in space.

The electric and magnetic nodes are arranged in space as shown in Figure 4.4. The x and y axes are indicated in the figure, and z axis is pointing out of the principle plane. The electric nodes are shown with black dots, and they are pointing out of the paper, polarized in the z direction. The magnetic nodes are shown with squares, with short lines indicating their polarization directions either in x or y axis. Every three field components E_z, H_x, and H_y in a node share a spatial index (m, n), and they are enclosed in a dashed line as shown in Figure 4.4. During simulation, the field values for these nodes are updated for every time step. Future values are solved for based on past values using the update equations obtained from equations 4.12-4.14, which are same as for the case of the one-dimensional simulation.

4.2.1 Simulated monolithic compressor structure

The preferred embodiment of the monolithic compressor has a Block 3 that is shaped as a heptahedron. When seen from the top (Figure 4.5), Block 3 is a pentagon that is symmetric with respect to a central line. As before, here grey represents fused silica, the green sides are distributed Bragg reflectors, and the yellow sides are metal reflectors. As stated in Chapter 3, the side reflectors on Block 2 must be distributed Bragg reflectors to avoid half-wave losses, but the rear reflectors on Block 3 can be made of metal. So here we use a metal reflector on the rear end of Block 3 for simplicity.

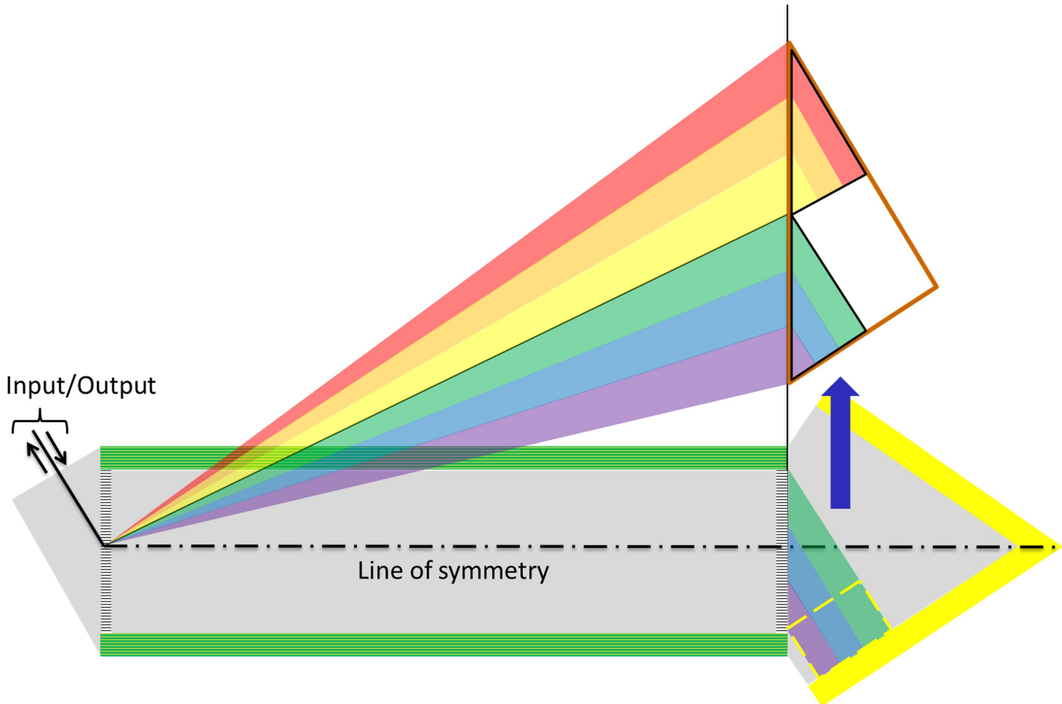

Figure 4.5 Experimental monolithic compressor device configuration.

As stated before, part of the beam trace enclosed in the yellow dashed square does not contribute to the optical path difference. This part will be ignored in the calculations; the optical path additions in Block 3 will therefore form saw-teeth-like shape. It appears that the two grey sides (Figure 4.5) of block 3 that form thesquare beam trace addition are not involved in either transmitting or reflecting light. A natural question that rises is: why do these two sides exist? The answer is that these two sides are necessary to account for mechanical tolerances. Block 3 is made from a bulk fused silica material that is polished to the desired shape. If these two sides were not there, then Block 3 would be a triangle, and it would be very difficult to fabricate with appropriate angles. With the two fused silica sides present, the two rear sides to be covered with metal reflectors can be polished to the desired best angles; thus the fused silica sides provide flexibility in the mechanical fabrication process.

In a mathematical simulation, however, there is no need to include these two sides because angles can be specified precisely and conveniently. To save computation time and memory, the structure in Figure 4.6 is employed in the simulation of the monolithic compressor.

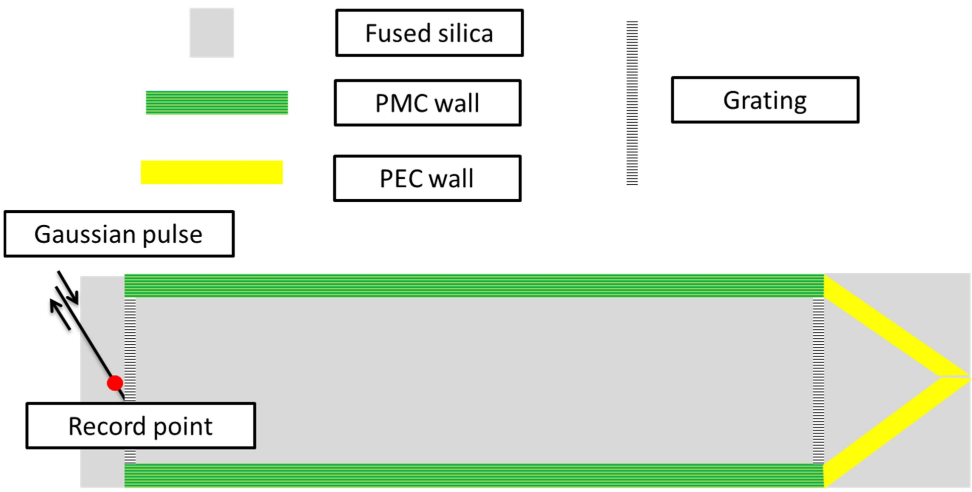

Figure 4.6 Simulation grid compressor implementation.

Here the first block is rectangular, and it is a solid fused silica material. Since the primary function of the first block is to balance the index of refraction difference between air and fused silica material, this implementation fulfills its task, and the interaction of the input pulse and compressor will not be changed. The input Gaussian pulse is introduced into the simulation grid at a vertical line that is a few steps away from the left-most boundary. This way, the reflection of input light between air and fused silica boundary is eliminated in the simulation. In an experimental situation, this would be achieved by coating the input surface of the first block with an anti-reflection coating.

Block 2 and 3 are also solid fused silica material, except for where the two gratings are present. These gratings are blazed to meet the Littrow condition, so they are simulated with little fused silica triangles with proper angles in the simulation grid. Since the grating constant is smaller than the central wavelength of interest, the smallest feature that needs to be discretized becomes the grating grooving. It is essential that the discretization be fine enough to distinguish the grating structure so that a reasonable diffraction effect can be achieved; we discuss this in detail in a following section.

The two reflectors in the monolithic compressor device are simulated as perfect conductors in the program. The distributed Bragg reflectors are simulated as perfect magnetic conductors (PMC), while metal reflectors are simulated as perfect electric conductors (PEC). In the following sections, we will demonstrate how these conductors serve the function of the corresponding reflectors.

As mentioned before, the third block is a solid fused silica. It actually does not matter what kind of material is on the right side of the metal reflectors because this part is out of the compressor region, and does not interact with any field. But for simplicity in implementation, we take it to be the same material as the rest part of Block 3.

As indicated in Figure 4.6 with the red dot, the electric field of the input source pulse is recorded at a position close to the first grating. After compression, the diffracted and compressed beams will follow their initial trace back to the original input point; so the electric field of the output pulse can also be recorded at the same spot. The recorded output and input fields will be compared and analyzed in a later section.

4.2.2 Oblique Gaussian pulse source

The input source in this simulation is a single Gaussian pulse that is obliquely incident onto the first grating in the compressor. It is introduced via a total-field/scattered-field (TFSF) boundary (Figure 4.7). There are mainly three ways of introducing source into the FDTD simulation grid: hard wired, additive source, and through a TFSF boundary. Hard writing (wiring) the source is undoubtedly the easiest method. But it has the big disadvantage that any field cannot get pass the source nodes. An additive source solves this problem, but the incident field cannot propagate in one direction. Only the field introduced through TFSF boundary can be designated to propagate in one direction, and in the meantime be transparent to any incoming field. We choose this type of field to introduce the pulse into the simulation. A TFSF boundary divides the simulation domain into two regions: the total field region which contains both the scattered filed and incident field; and the scattered field region which only contains the scattered filed.

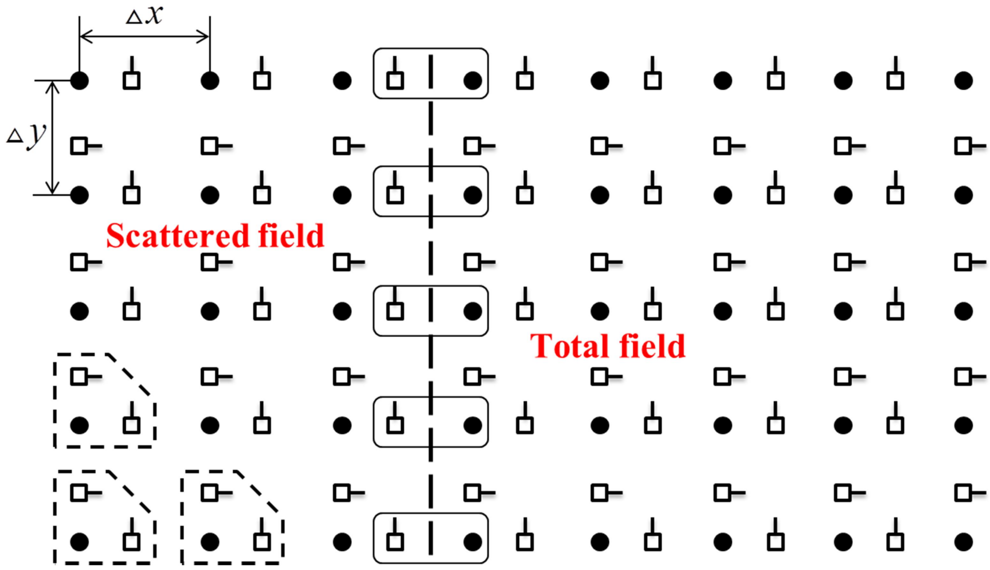

Figure 4.7 2D total-field/scattered-field (TFSF) boundary.

As shown in Figure 4.7, the TFSF boundary in this simulation is a straight line that lies in parallel with the y axis (indicated with the dashed line). The scattered field region is to the left of this boundary, while the total field region is to the right of this boundary. Any node that has a neighbor on the other side of the TFSF boundary needs to be corrected. Note that these nodes are all tangential to the TFSF boundary. The E_z and H_y nodes to be corrected are enclosed with a solid rectangle with rounded corners. The input field must be known at all these nodes and for every time-step. To account for the input source, the incident field is subtracted from corresponding neighboring node for all H_y nodes on the left of the TFSF boundary. Conversely, for the update of all E_z nodes, the incident field is added to the neighboring node on the other side of boundary.

In this simulation, an auxiliary two dimensional grid (lower portion of Figure 4.8) is constructed to model the propagation of the incident wave. It has the same dimension as the main simulation grid in the y axis, and a shorter size in the x direction. It uses the same Courant number as the main grid, but is otherwise completely separate from the main grid. The only function of this auxiliary grid is to provide field values of the incident source; the nodes adjacent to TFSF boundary in the main grid can thus be updated.

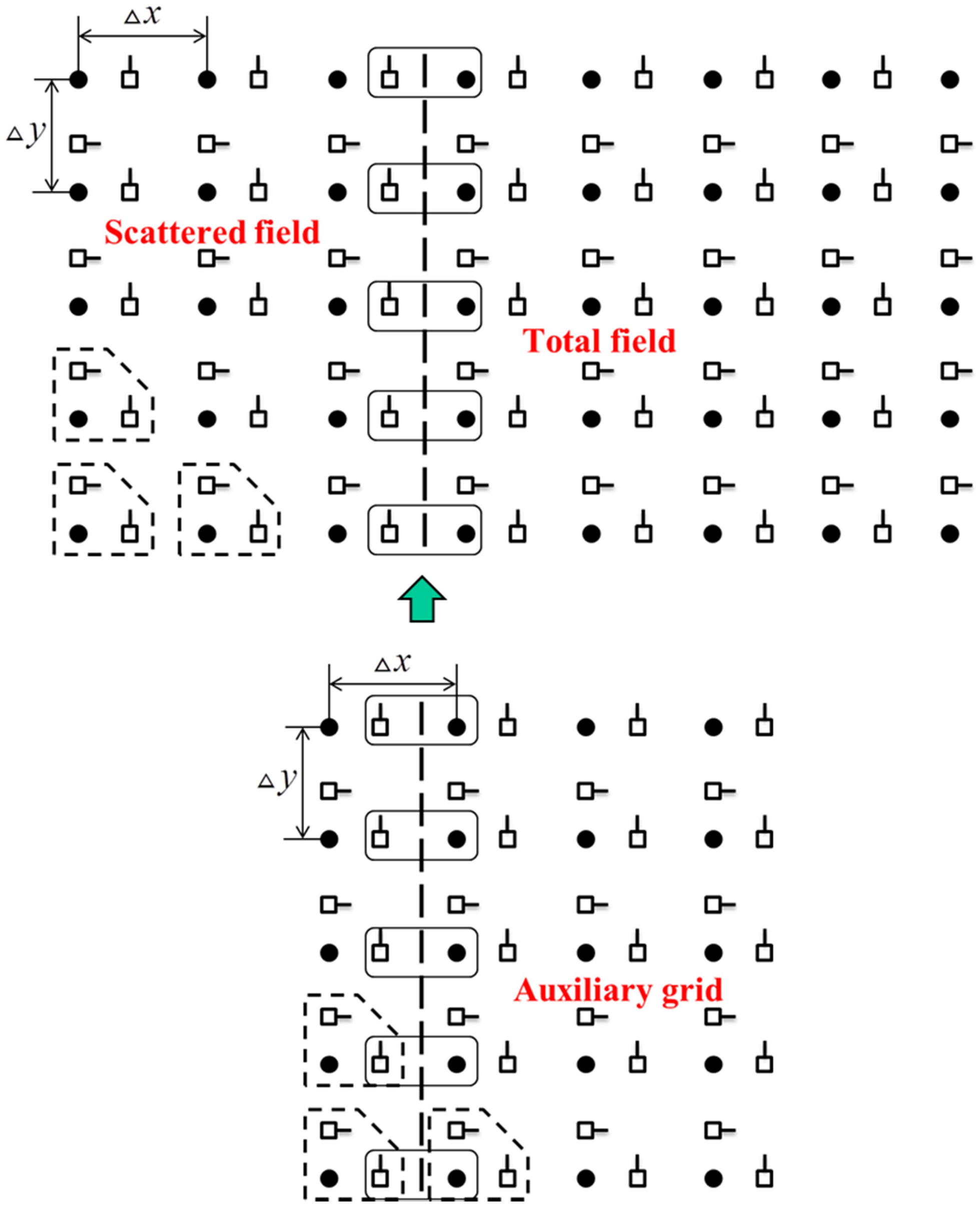

Figure 4.8 2D total-field/scattered-field (TFSF) boundary and auxiliary 2D source grid.

The incident Gaussian pulse is hard written (wired) on the left boundary of the auxiliary grid, and updated in the same manner as the main grid. The incident field will propagate to the right until it is absorbed by the boundary. Except for the left boundary where the incident field is written (wired), all the other three boundaries are properly terminated so that any incoming field will not be reflected back into the grid. As indicated with the dashed line in the lower part of Figure 4.8, the H_y and E_z

fields one cell away from the left boundary (enclosed with solid rectangle with rounded corners) are recorded and used in updating the corresponding nodes on the sides of the TFSF boundary in the main grid. The TFSF boundary in the main grid can be chosen to be anywhere in theory, but here we assume it is a few cells away from the left boundary because it will be sent into the compressor system on the right.

The complex form of the transform-limited Gaussian pulse written (wired) at the left boundary of the auxiliary grid is:

$$\begin{aligned} \mathrm{U(r,z,t)} &= \frac{w_0}{w(z)}\exp\left[-1.38\frac{t^2}{t_0^2}\right]\exp\left[-\frac{r^2}{w(z)^2}+\frac{r^4}{2w(z)^4}\left(\frac{1}{t_0\omega_0}\right)^2\right] \\ &\times\exp\left\{i\omega_0\left[1-\frac{r^2}{w(z)^2}\left(\frac{1}{t_0\omega_0}\right)^2\right]+i\varphi(z)\right\}, \end{aligned} \tag{4.15}$$

with

$$w^2(z) = w_0^{\ 2}\left[1+\left(\frac{z}{z_0}\right)^2\right]; \tag{4.16}$$

$$\varphi(z) = \tan^{-1}\left(\frac{z}{z_0}\right); \tag{4.17}$$

$$z_0 = \frac{\pi w_0^2}{\lambda_0}. \tag{4.18}$$

Here w_0 is the waist size of the beam, while the parameter $w(z)$ describes the variation of the beam profile along the axis of the beam and is called the beam waist. In this general form, the axis of the beam lies in the z direction, and r defines the transverse distance from the beam axis. In the simulation grid, the x axis represents z in equation 4.15, while y stands for r; t_0 is the 1/e pulse width in the time domain, and ω_0 is the carrier frequency of the pulse; z_0 is known as the Rayleigh length, which is the length the beam can propagate without significantly diverging.

The electric field E_z is obtained by taking the real part of equation 4.15. To avoid rapid change, the input source is delayed for $3t_0$ time steps before entering the grid. By applying the Gaussian pulse to the left boundary of the auxiliary grid, updating the TFSF boundary nodes in the main grid using the recorded values, a normal incident transform-limited Gaussian pulse can be generated. The snapshots taken of the electric field at different time steps are shown in Figure 4.9.

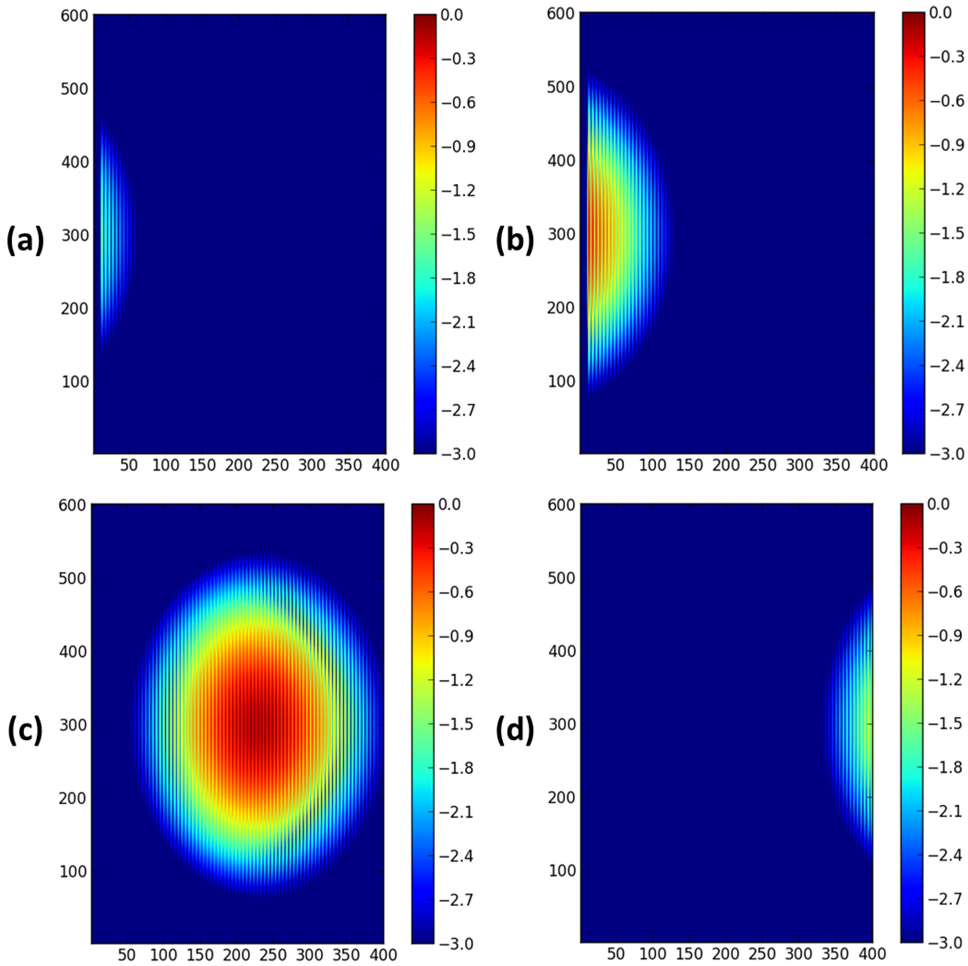

Figure 4.9 Snapshots of electric field in main grid at time steps: (a) 100, (b) 200, (c) 600, and (d) 1000. The indices shown are corresponding spatial indices of the FDTD grid. Shown magnitude is logarithmic scale of the real electric field: 0 stands for 1, while -3 stands for 0.001.

The field is introduced into the main grid 10 cells away from the left boundary, and propagates straight to right without a perceived divergence. The beam waist is made nine times size of the pulse central wavelength. A full clean Gaussian pulse can be observed in Figure 4.9 (c).

In FDTD simulations, it has always been tricky to implement an oblique source. Here, instead of changing the expression of Gaussian pulse (equation 4.15) itself, the beam axis is rotated with respect to the x axis of auxiliary grid. This way, different incident angles can be achieved conveniently without altering the Gaussian pulse expression itself.

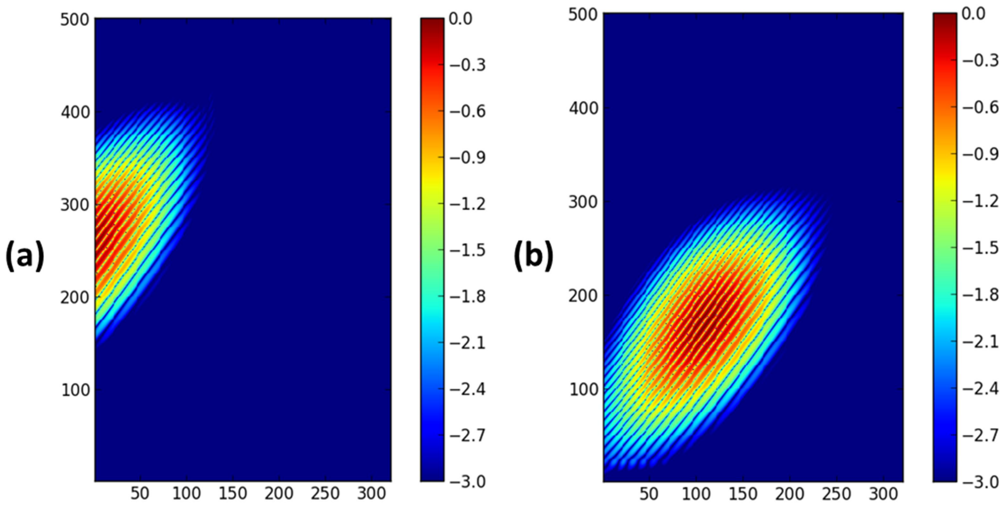

Figure 4.10 Snapshots of electric field in auxiliary grid at time steps: (a) 300, and (b) 600. The indices shown are corresponding spatial indices of the auxiliary grid. Shown magnitude is logarithmic scale of the real electric field: 0 stands for 1, while -3 stands for 0.001.

Figure 4.10 illustrates an oblique Gaussian pulse with an incident angle of 45 degrees. It consists of the snapshots of electric field in the auxiliary grid at two different time steps. One records the field one cell away from the left boundary and uses it to update the main grid, a TFSF-introduced oblique Gaussian pulse source can be generated with the same pulse shape.

4.2.3 PEC and PMC

As stated earlier, metal reflectors on the rear end of the compressor are simulated as perfect electric conductors (PEC), and the distributed Brag reflectors on the side surfaces of the compressor main body are simulated as perfect magnetic conductors (PMC). The decision for the different kinds of reflectors used on separate sides of different blocks of the compressor is based on an evaluation of the optical pulse interaction with the surface and on the ease of implementation. Since PEC is easy to define and implement, it can be used to stand for a perfect metal reflector. However, it will cause half-wave loss. Thus on the side walls of block 2 of the compressor, we use PMC to function as a perfect but simple version of the distributed Bragg reflector. To verify the half-wave-loss-free reflection at PMCs, an illustrative example of the recorded electric field of the pulse for both PMC and PEC reflection will be put together in the following paragraphs.

Perfect electric conductors (PECs) are materials whose conductivity is assumed to approach infinity. If the fields were non-zero in a PEC, that would imply the current was infinite. Since infinite currents are not allowed, the fields inside a PEC are required to be zero. This subsequently requires that all points of the PEC must be at the same potential. So a PEC acting like a perfect metal material causes all fields reflected by the PEC to suffer what is called a half-wave loss.

A perfect magnetic conductor (PMC) on the other hand, is a high-permeability material. It doesn't let magnetic fields penetrate; it is thus an ideal magnetic shield. The magnetic field node in a PMC boundary is initially zero and remains zero throughout the simulation. When the field encounters these nodes, a reflected wave is created which reverses the sign of the magnetic field but preserves the sign of the electric field. This way, no half-wave loss is created, and the incident pulse is reflected as it encounters a perfect distributed Bragg reflector.

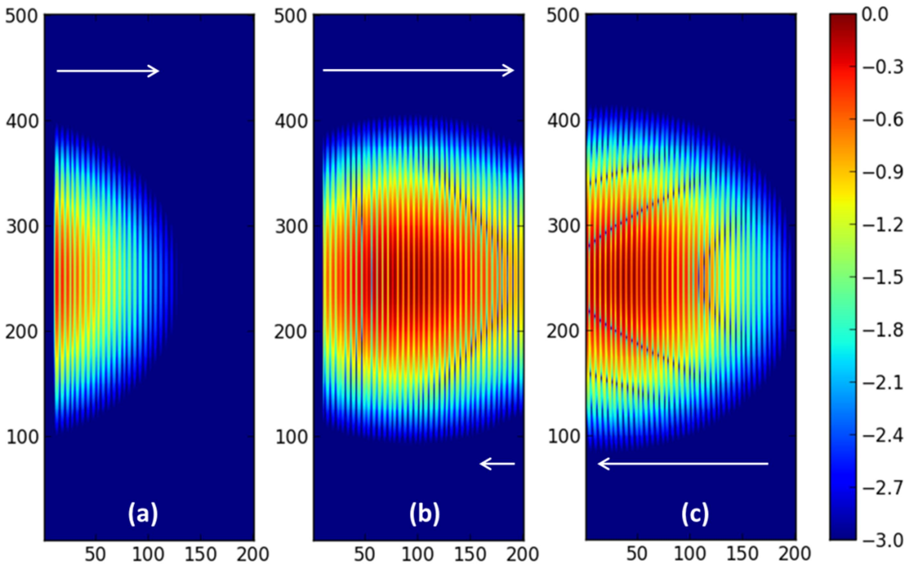

Figure 4.11 Snapshots of normal Gaussian pulse reflected by PEC wall. (a) pure incident pulse, (b) partial reflected, and (c) fully reflected pulse. The indices shown are spatial indices of the grid. Shown magnitude is logarithmic scale of the real electric field: 0 stands for 1, while -3 stands for 0.001.

Snapshots of the simulation grid where a PEC wall is present at the right boundary are illustrated in Figure 4.11. The Gaussian pulse is introduced into the grid via TFSF boundary, so the reflected field can pass through the source nodes. The incident Gaussian pulse starts from the left (Figure 4.11(a)), and propagates to the right until it impinges on the PEC wall (Figure 4.11 (b)). Then the reflected pulse reverses its propagation direction, and moves to the left until it gets absorbed by the boundary (Figure 4.11 (c)). If the PEC wall on right is replaced by a PMC boundary, snapshots of the same grid will have slight changes regarding the reflected pulse phase, but those changes are hardly observable.

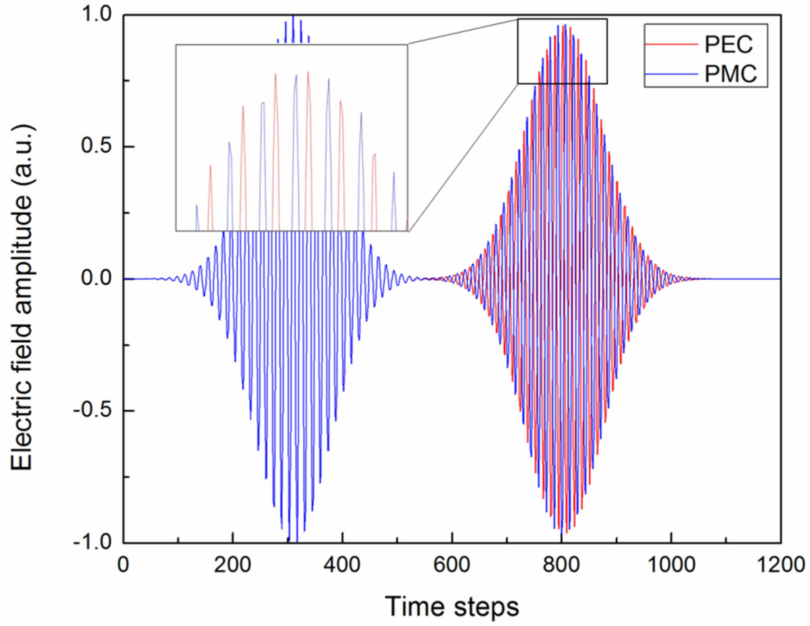

Figure 4.12 Recorded electric field amplitudes of Gaussian pulse reflected by PEC/PMC walls.

Shown in Figure 4.12 are the recorded electric fields for both the incident (on the left) and reflected (on the right) Gaussian pulse obtained from PEC and PMC reflection put together. The simulation grid and input Gaussian pulse parameters are all the same for the PEC and PMC reflection simulations. The only difference between these two simulations is the reflector definition. The electric field is recorded 30 cells away from the left boundary of the simulation grid shown in Figure 4.11. Red lines represent electric field recorded for the PEC wall refection simulation, while blue lines stand for the PMC boundary reflection.

Since the input source is the same for these two simulations, the pulse shapes on the left overlap, and we see a single clear Gaussian pulse. On the right side, however, the blue and red lines get separated. This is because the PEC reflection causes a half-wave loss, while the PMC reflection does not. This phenomenon is especially obvious at the pulse maximum as shown in the zoomed-in illustration.

4.2.4 Blazed grating structure

In order to have the maximum energy diffracted at the first order, the grating must be blazed at a proper angle. The grooving of a blazed grating has a triangular shape. Since the grating constant to be used in this simulation is 600 nm, while the central wavelength is 1030 nm, the grating grooving becomes the smallest feature that needs to be discretized. To make sure that the grating can disperse the input source properly, different points per wavelength (PPW) values are tested.

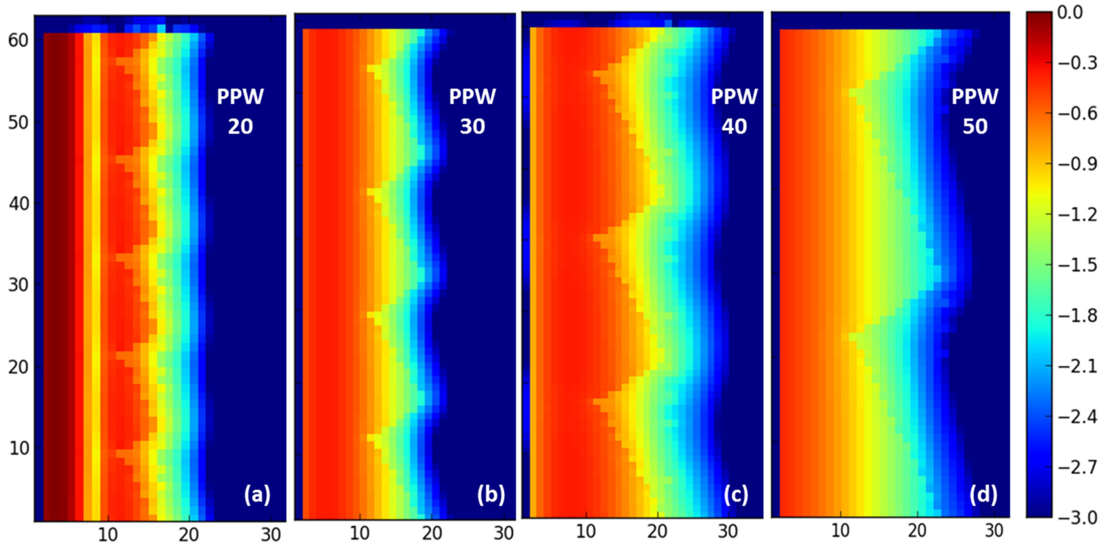

Figure 4.13 Snapshots of normal plane wave diffracted by blazed grating. Four different discretization levels are used, and points per wavelength equals: (a)20, (b) 30, (c) 40, and (d) 50, respectively. The indices shown are spatial indices of the grid. Shown magnitude is logarithmic scale of the real electric field: 0 stands for 1, while -3 stands for 0.001.

To better appreciate the grating structure itself, the input source is set to be a plane wave centered at 1030 nm. The source is introduced via the TFSF boundary, and stays the same for all four of these simulations. For the first case (Figure 4.13 (a)) where the points per wavelength (1030 nm) equal 20, there are 12 points per grating constant

(600 nm). Similarly, the parameter "points per grating constant" is 17, 23, and 29 for discretization level (points per wavelength) of 30, 40, and 50, respectively. So for the same size dimension in y axis, different numbers of grooving appear in corresponding discretization levels. As can be seen from Figure 4.13, the highest discretization level, where points per wavelength equal 50, gives the best diffraction effect. As the discretization level becomes coarser from 50 to 20, the diffraction effect gets poorer, accordingly. When points per wavelength equal 30, it gives an acceptable diffraction effect with the least points needed to discretize the grating structure.

4.3 Monolithic compressor simulation results

With all necessary elements prepared (input source, reflectors, and grating structure), we are now ready to simulate the monolithic compressor. A proper set of parameters for the compressor in the simulation grid is chosen first. As a consequence, the amount of dispersion is settled as well. Thus the pulse width of input source can be traced from the given dimensional parameters.

We present illustrations of electric field propagation traces, and an analysis of the corresponding output pulse shape. Both of these two forms of output validate our previous analysis of the monolithic compressor. Although the output results use standard fiber system parameters, these can be scaled to any dimensions to reflect pulse compression effects of different systems.

4.3.1 Compressor system parameters

The finite-difference time-domain (FDTD) method is a powerful but computationally expensive simulation method. This is the main reason that although the method was first conceived by Yee in 1966 [32], it did not get much attention until high-speed computers became available later.

Although there is no intrinsic limit on how many field unknowns an FDTD program can simulate, a large simulation grid will be extremely slow and cost too much computational time and resources. As has been tested, simulations with the same discretization but different sizes give the same pulse shape result. The only difference is the compression ratio. Thus instead of simulating the full size monolithic compressor with dimensions of several centimeters [34], which is unnecessary and unrealistic, a scaled-down compressor with dimensions in the one hundred micrometer regime is constructed and simulated (Figure 4.14).

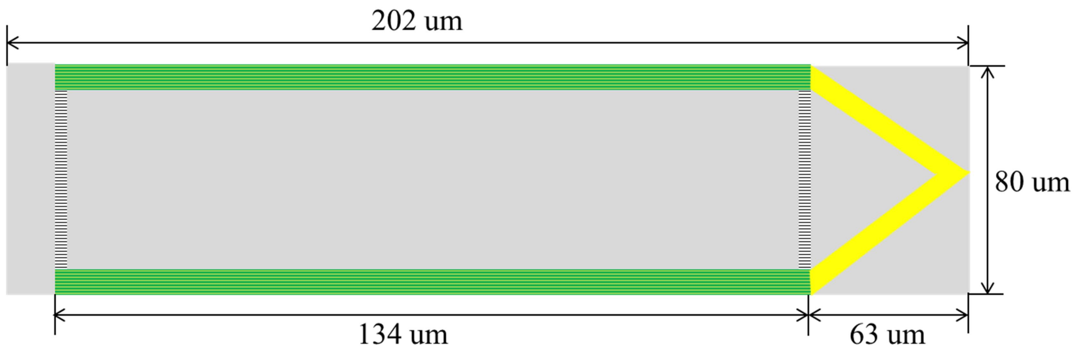

Figure 4.14 Dimensions of simulated monolithic compressor.

The discretization level used for this simulation is 30 points per wavelength. This means there are 17 points per grating constant, and it is the least points that is capable of generating satisfying diffraction effects (as discussed in Section 4.2.4). With the central wavelength being 1030 nm, one spatial cell stands for 34.33 nm. The grating width is 80 μm, and the separation between the gratings is 134 μm. The Courant number, $S_c = c\Delta\text{t}/\Delta\text{x}$, is set to be the maximum value $1/\sqrt{2}$. According to this, the unit temporal step size equals $8.1 \times 10^{-17}\ s$. This is more than enough to discretize the input pulse, so the smallest feature that needs to be discretized remains the grating grooving (grating constant equals 600 nm). The simulation is considered accurate as long as the grating grooving is discretized finely enough.

4.3.2 Dispersion pre-compensated source

Before exploring the nature of the pulse compression technique, it is essential that we understand the laser source that the system takes in. The Gaussian pulses shown and discussed previously are transform-limited, which means that they have the minimum pulse duration possible for a corresponding optical bandwidth. A transform-limited pulse cannot be compressed, what can be compressed are called chirped Gaussian pulses, and the chirp can be introduced via dispersion or nonlinear effects.

The source Gaussian pulse used for this simulation is pre-compensated for the dispersion that will occur in the compressor. In other words, the input pulse is manually chirped to have positive group velocity dispersion. At this stage, the dispersion profile of the monolithic compressor system is still unclear. So the input pulse is assumed to have a linear positive chirp, as it is usually the case after being stretched by a standard single mode fiber.

The linearly chirped Gaussian pulse has a similar expression as stated in equation 4.15. The biggest difference is the addition of a chirp parameter C:

$$\mathrm{U(r,z,t)} = \frac{w_0}{w(z)}\exp\left[-1.38\frac{(1-iC)t^2}{outt_0^2}\right]\exp\left[-\frac{r^2}{w(z)^2}+\frac{r^4}{2w(z)^4}\left(\frac{1}{t_0\omega_0}\right)^2\right]$$
$$\times\exp\left\{i\omega_0\left[1-\frac{r^2}{w(z)^2}\left(\frac{1}{t_0\omega_0}\right)^2\right]+i\varphi(z)\right\}. \tag{4.19}$$

C is defined as:

$$C=\sqrt{\left(\frac{2\pi\Delta\lambda outt_0}{\sqrt{1.38}\lambda_0^2}\right)^2-1}. \tag{4.20}$$

The other parameters are the same as defined in equations 4.16-4.18. The linearly and positively chirped Gaussian pulse has a phase distribution as illustrated in Figure 4.15. Note that the instantaneous frequency increases linearly with time.

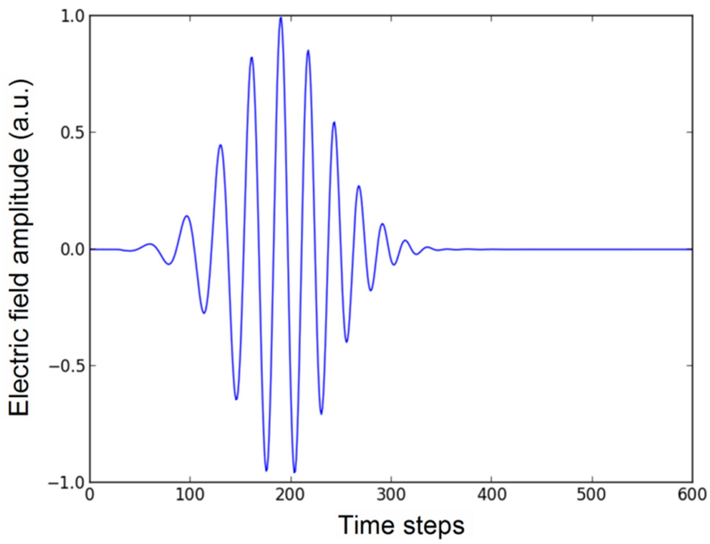

Figure 4.15 Electric field amplitude of a typical positively and linearly chirped Gaussian pulse.

The input Gaussian pulse used in this simulation has the same shape as shown in

Figure 4.15, but with a much longer duration. To take full advantage of the gain bandwidth of the amplifier medium, which is a Ytterbium-doped fiber in this project, the input pulse bandwidth is set to be 80 nm. Thus the corresponding duration for a transform-limited Gaussian pulse is 20 fs. Given the compressor parameters set for the simulation grid in section 4.3.1, the total amount of dispersion is already fixed. Assume that the input chirped pulse is compressed to its shortest duration after a round trip in the simulated compressor, the input pulse duration can be traced back from equations 3.30 and 3.31 as 0.6 ps.

The given set of parameters for the input source ensure that the pulse can be compressed to a desired duration, but the pulse shape, or dispersion profile, has not been taken into consideration. In order to have a clean compressed output pulse, the response of the given compressor to a linearly chirped input source should be simulated first. Then based on the output pulse of compressor, a nonlinearly chirped fiber Bragg grating stretcher should be properly designed. This way, the dispersion profiles of the stretcher and compressor match with each other, and the dispersion of the monolithic compressor can be fully compensated.

4.3.3 Electric field plots

With the simulation grid defined in Section 4.3.1 and the input chirped Gaussian pulse described in Section 4.3.2, the electric field amplitudes inside the monolithic compressor can be plotted as shown in Figure 4.16-4.18. Note that the input Gaussian pulse is introduced via a total field/scattered field (TFSF) boundary located 5 cells away from the left boundary, and it is incident on the first grating of the compressor at an angle of 59.13 degrees.

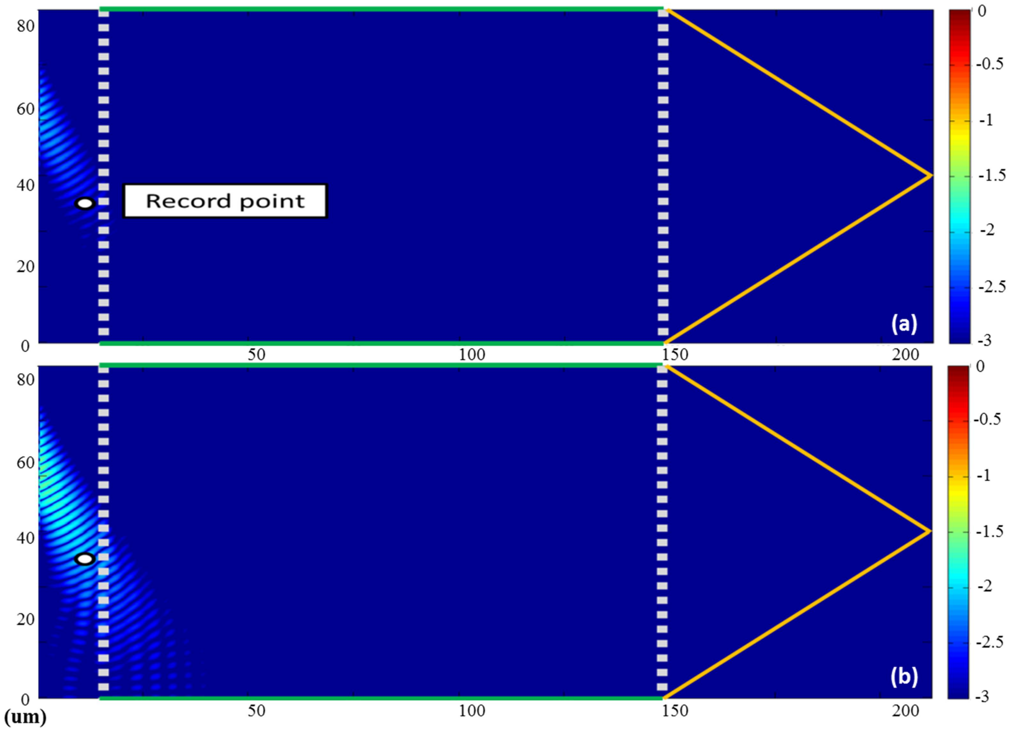

Figure 4.16 Snapshots of simulated electric field inside monolithic compressor. (a) Input Gaussian pulse before impinging on the grating. (b) Gaussian pulse get diffracted by the first grating in compressor. The indices shown are spatial dimensions of the grid. Shown magnitude is logarithmic scale of the real electric field: 0 stands for 1, while -3 stands for 0.001.

Illustrated in Figure 4.16 (a) is the situation where the oblique input chirped Gaussian pulse has not arrived on the grating yet. Since the pulse is chirped and has a long duration, only part of the pulse is shown here. The two dashed light grey lines stand for the two integrated gratings in the monolithic compressor. The solid green lines on the top and bottom of the simulation grid represent distributed Bragg reflectors, while the yellow lines on the right rear end represent metal (such as gold) reflectors. The electric field recording point is placed on the left of the first grating in the compressor, and both the input and output pulses can be recorded at the same point. These notations will stay the same for all illustrations in Figure 4.16-4.18.

In Figure 4.16 (b), the input pulse impinges on the first grating in the monolithic compressor and gets diffracted by it. It is obvious that some portion of the pulse is reflected, while the majority gets passed through. Both the reflected and transmitted fields are diffracted to different directions according to different wavelengths. Because of the blazed grating structure, most energy of the transmitted field is diffracted at the -1 order as illustrated. Note that the reflection can be eliminated in an experiment by using anti-reflection coatings.

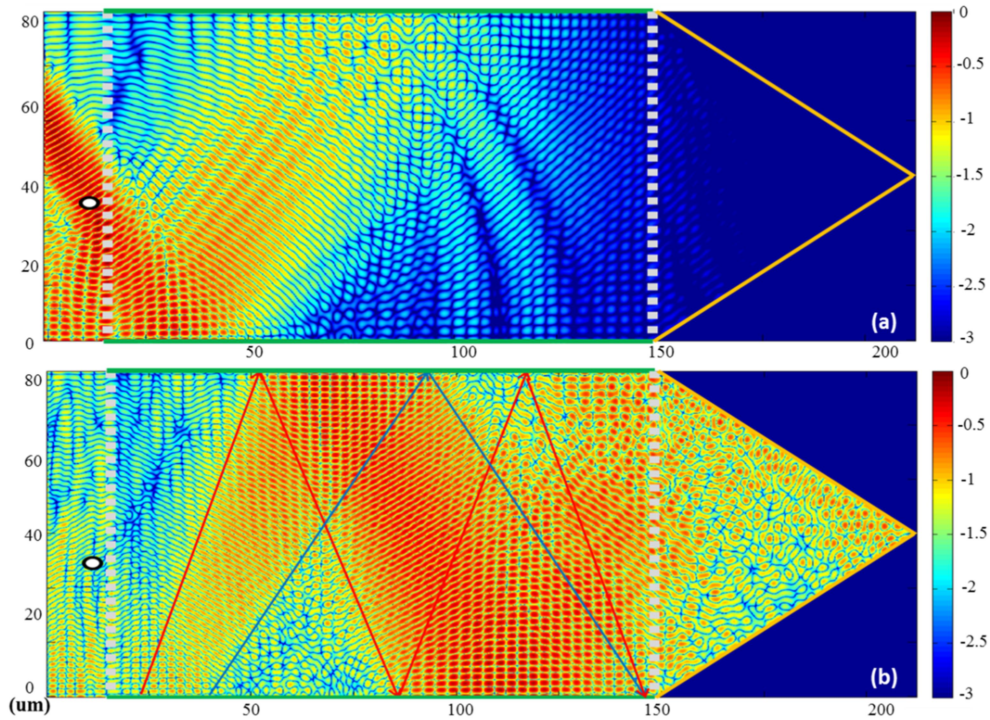

Figure 4.17 Snapshots of simulated electric field inside monolithic compressor. (a) Transmitted Gaussian pulse gets reflected by side reflectors. (b) Full beam propagation trace of transmitted Gaussian pulse inside monolithic compressor before impinging on the second grating. The indices shown are spatial dimensions of the grid. Shown magnitude is logarithmic scale of the real electric field: 0 stands for 1, while -3 stands for 0.001.

After diffraction by the first grating, the transmitted field keeps propagating, and it encounters the side reflectors on the side surfaces of block 2 in the compressor (Figure 4.17 (a)). The transmitted field is thus folded back into the block, and is bounced back and forth as it propagates toward the second grating in the compressor. At this stage, the angular spread of the transmitted beam caused by diffraction is even more obvious. Different wavelength components in the beam follow different paths (as indicated in Figure 4.17 (a)).

Illustrated in Figure 4.17 (b) is the situation where the transmitted field has just arrived at the second grating. Also, here the input pulse has finished passing through the first grating. The beam propagation traces of selected wavelengths in the transmitted field are indicated with red and blue arrows. Red represents the longest wavelength component, while blue indicates the shortest wavelength component. Note that here the compressor is designed to have a two-fold structure, in other words, the divergence of the diffracted beam, when arriving at the second grating, should be twice as large as the grating width (which equals the simulation grid width here). Thus starting from the left, where the red and blue arrows begin, the shortest wavelength component (blue) gets reflected by the side reflectors for twice (the second reflection is not obvious because it happens just on the left of the second grating), while the longest wavelength component (red) gets reflected by the side reflectors for three times.

Since the beam divergence is twice the grating width, we can divide the diffracted beam into two bands: the lower band which contains the shortest wavelength component, and the upper band which contains the longest wavelength in the pulse. The lower band arrives at the second grating after reflection by the side reflector at the bottom, that is to say, it will impinge on the second grating in an oblique upward direction. The upper band, on the other hand, arrives at the second grating after reflection by the side reflector at top. It will impinge on the second grating in an oblique downward direction. The beam interactions with the second grating are shown in Figure 4.18.

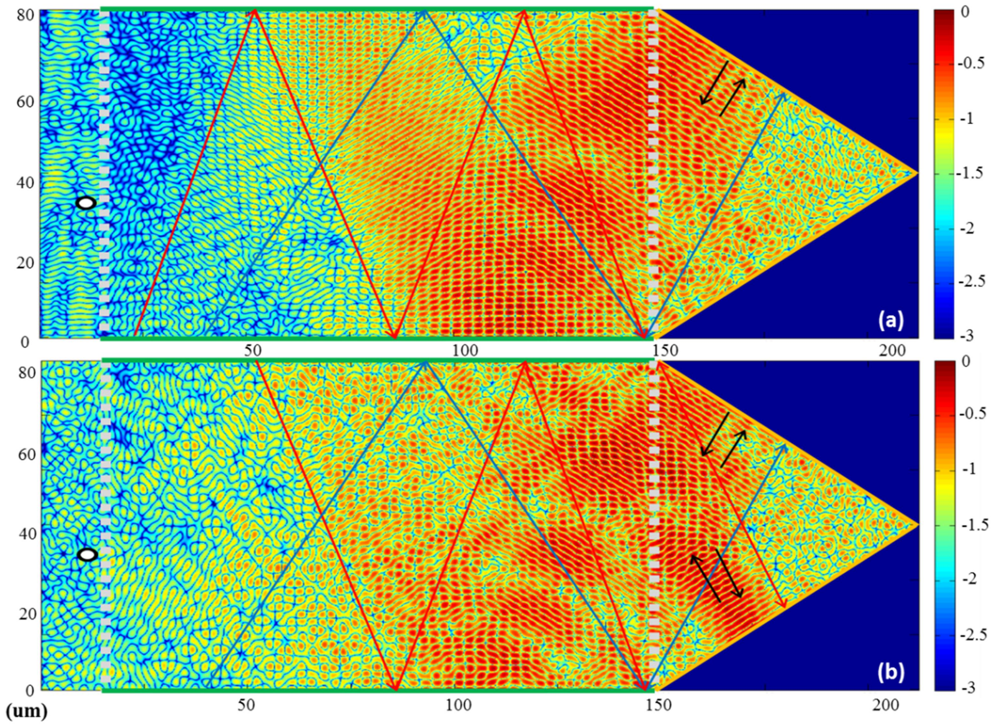

Figure 4.18 Snapshots of simulated electric field inside monolithic compressor. (a) Only the lower band of transmitted pulse passes through the second grating and gets reflected by rear reflectors. (b) Both the lower and upper bands of transmitted pulse passes through the second grating and gets reflected by rear reflectors. The indices shown are spatial dimensions of the grid. Shown magnitude is logarithmic scale of the real electric field: 0 stands for 1, while -3 stands for 0.001.

Since the lower band of beam travels for a shorter distance, it arrives at the second grating at an earlier time than the upper band. Shown in Figure 4.18 (a) is the case where the lower band has passed through the second grating, while the upper band hasn't. Upon impinging on the second grating, the lower band is diffracted at a direction that is a mirror symmetry of the incident source beam with respect to the center line of Block 2 of the compressor. Its direction of propagating is perpendicular to the rear mirror at the right end of Block 3. Thus the retro-reflected beam follows the same path that it came in on, and returns to its initial starting point.

In Figure 4.18 (b), the upper band of the beam also gets passed through the second grating. It is diffracted at a direction that is parallel to the incident source beam, and has a mirror symmetry with the direction of the lower band of the beam with respect to the Block 2 central symmetry line. Again, this band is propagating perpendicularly to the rear mirror in Block 3 (indicated with red arrow). Thus it gets retro-reflected following the same path it came in on.

The simulated electric field plots indicate that the monolithic compressor is interacting with the incident stretched pulse just the way we expected it to. The obliquely incident Gaussian pulse gets angularly spread out after diffraction by the first grating in the compressor. The side reflectors fold the diffracted beam back into Block 2 as it propagates toward the second grating. Different wavelength components are reflected for different number of times. In this case, the wavelength components in the upper band are reflected for three times, while the wavelength components in the lower band are reflected twice. The second grating re-collimates the bands of light into parallel beams. Although the two bands have different directions of propagation, they are symmetric with respect to the central line in Block 2. Thus they can both be retro-reflected by the rear mirrors in Block 3, which are perpendicular to the beam bands directions of propagation, respectively. The input and output pulses are recorded at the same point, and they are analyzed in the next section.

4.3.4 Output compressed pulse

The recorded electric fields of the input and output pulses, along with the corresponding envelopes, are plotted in Figure 4.19. Figure 4.19 (a) is the linearly chirped Gaussian pulse source with a stretched total temporal duration of 2 ps. The corresponding full-width at half-maximum intensity pulse width is 0.6 ps. The input is normalized to have unit maximum amplitude.

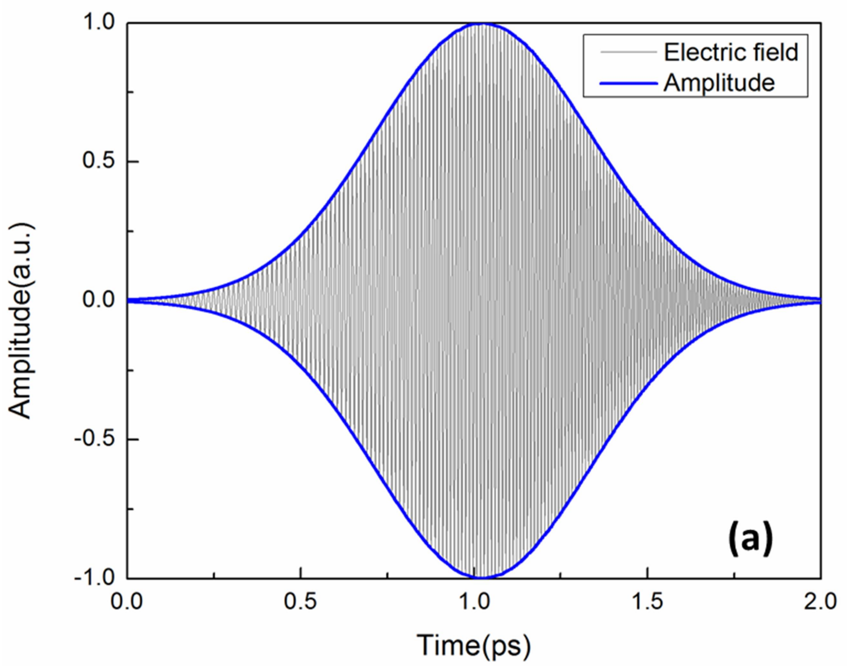

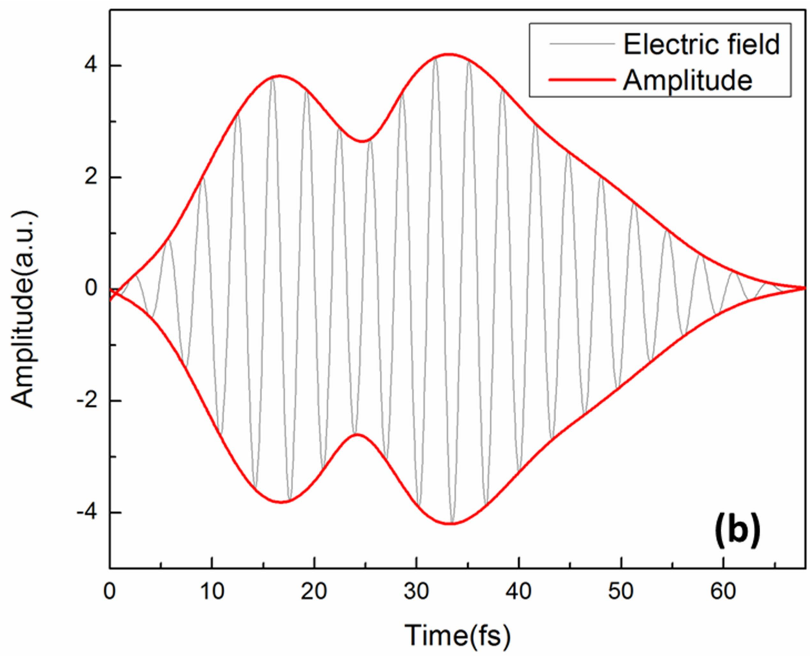

Figure 4.19 Electric field amplitude of: (a) linearly chirped Gaussian pulse source; and (b) output pulse with depression in middle.

The output, shown in Figure 4.19 (b), is a Gaussian pulse with a depression in the middle. As can be seen from the plot, the initial chirp does not exist anymore. The instantaneous frequency stays the same throughout the pulse, indicating that the pulse has been compressed close to its shortest duration. The compressed pulse has a total duration of 70 fs, and a corresponding pulse width of 25 fs.

The reason why there is a depression in the pulse amplitude can be found by referring to the monolithic compressor configuration that is illustrated in Figure 4.20; this illustration of the monolithic compressor also shows beam propagation traces for selected wavelength components of the input pulse. The solid black line represents the input/output beam. The two dashed black triangles represent the optical path additions after the second grating for the two bands of the diffracted beam; each has a side equal to the grating width W. Red lines indicate the beam propagation trace for the longest wavelength component, while green is the central wavelength, and purple stands for the shortest wavelength.

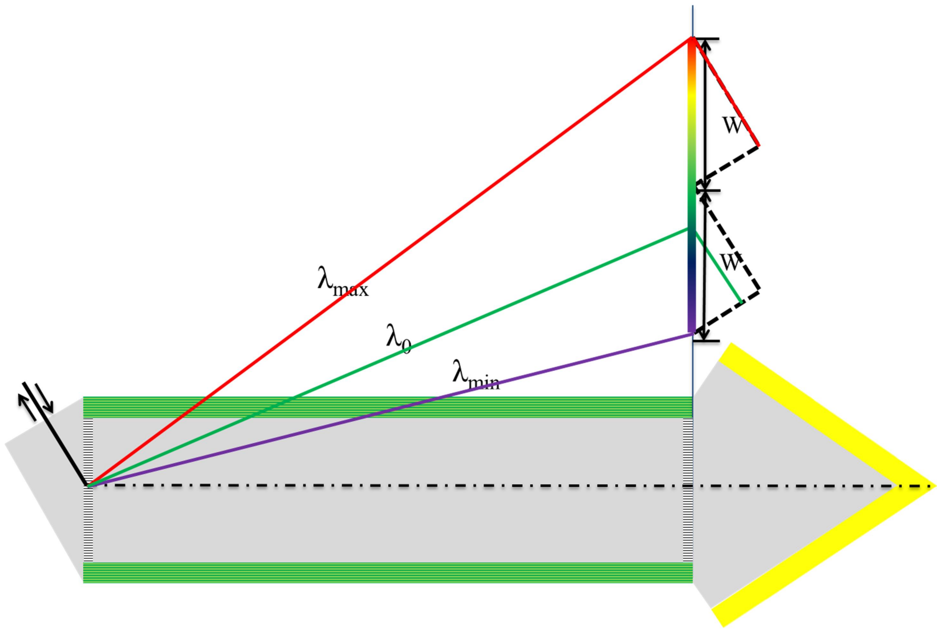

Figure 4.20 Monolithic compressor with beam propagation trace of selected wavelengths.

As explained before, the optical path additions after the second grating are not continuous for all wavelength components. There is an abrupt change in the middle of the beam divergence, or in other words, at the point where the two little dashed triangles ("saw teeth") touch as indicated in Figure 4.20. This will naturally cause the compressed pulse to be split up. However, as can be seen from Figure 4.19 (b), the depression does not happen right in the middle. Instead, the lower band, which contains the shortest wavelength component, appears to have more short wavelength component content. This is actually easy to understand. As indicated in Figure 4.20, the beam divergence, and the compressor parameters, are decided based on the separation between the longest and shortest wavelength components. According to the grating equation, the central wavelength of the pulse is actually diffracted at an angle that is closer to the shortest wavelength than the longest one. This is illustrated in

Figure 4.20. Thus the lower band contains more wavelength components than the upper band, and the output pulse has a shape as plotted in Figure 4.19 (b).

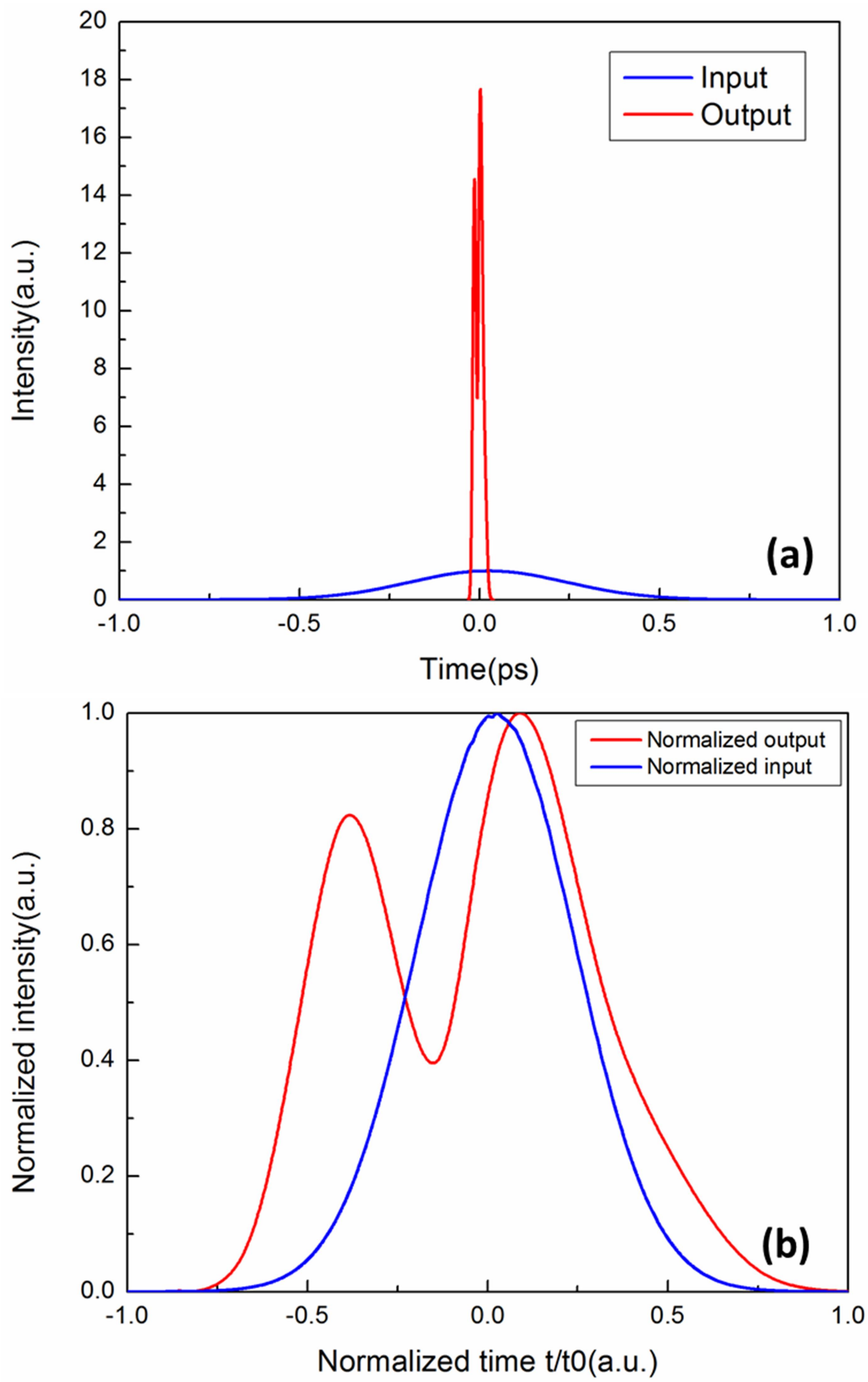

Figure 4.21 (a) Field intensity of input can output pulses; and (b) Corresponding normalized field intensity.

The field intensity of the input and output pulses is shown in Figure 4.21 (a). The output pulse is temporally compressed to a much shorter pulse width than the input, and its field intensity is 18 times as large as the input pulse. Since it is difficult to see the pulse details in the normal scale, a normalized time and intensity plot is generated (Figure 4.21 (b)). From this figure, we can see clearly that the output pulse has a Gaussian shape. It gets split up because of the saw-teeth optical path addition after the second grating in the monolithic compressor, and a depression forms. The left part (corresponding to the upper band of the pulse) has fewer wavelength components, while the right part (corresponding to the lower band of the pulse) has more wavelength components.

Knowing the response of the compressor to a linearly chirped Gaussian pulse input, one can now design a matching nonlinearly chirped fiber Bragg grating. Since the dispersion profile of a fiber Bragg grating can be devised to have any desired shape, we can make it so that it has a saw-tooth optical path addition that cancels out the dispersion of the monolithic compressor. Using this fiber Bragg grating as the stretcher together with the new monolithic compressor as the matching compressor, clean ultra-short and high-peak-power laser pulses can be produced.

4.4 Compressed pulse possible improvement

Although the depression in the compressed pulses can be compensated for by a properly designed nonlinear fiber Bragg grating, looking into other solutions to reduce the depression can still be helpful in giving us a deeper understanding of the operation of the monolithic compressor.

One way to reduce the depression in the simulation is to increase the discretization level. For our simulation, the parameter points per wavelength equals 30, and the Courant number is $1/\sqrt{2}$. This leads to a simulation accuracy of 99.71%, which corresponds to an error of 0.29%. If we increase the parameter points per wavelength, more wavelength components can be identified with increasing discretization level. The pulse will be filled with more wavelength components so that their intensities overlap to make the depression smaller. But this would only lead to a small depth change, because our discretization is already approaching the saturation limit as shown in Figure 4.22.

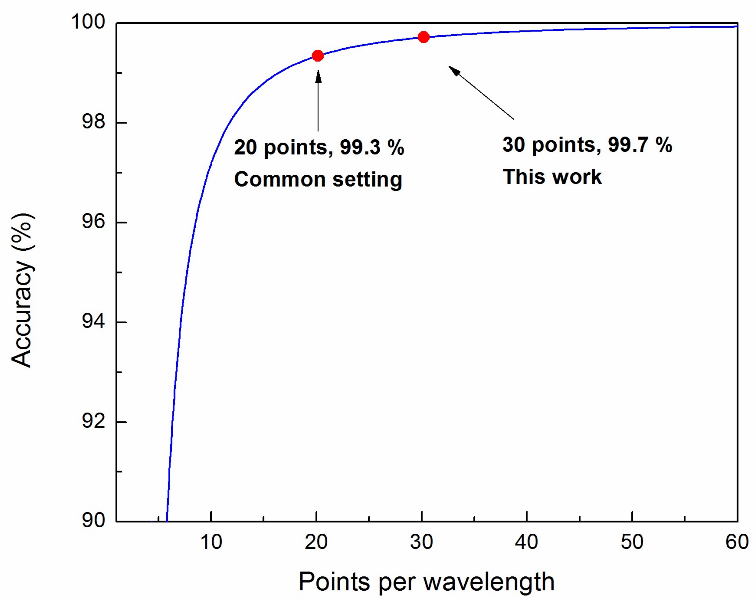

Figure 4.22 Simulation accuracy as a function of discretization level (points per wavelength).

The second way is related to the physical structure of the monolithic compressor. That is, the depression can be reduced by making the transverse size of the compressor to have more than twice the size of the grating. In other words, the beam divergence of the diffracted field after the first grating can be more than twice the size of the grating width. This way, there will be more saw-tooth like optical path additions after the second grating of the compressor, and the optical path difference between different bands of the diverged beam can therefore be reduced. Correspondingly, there will be more depressions in the output compressed pulse, but each depression will be reduced compared to the compressor with the two-fold width structure with the same compression ratio.

5. Summary and outlook

An ultra-compact grating-based monolithic optical pulse compressor has been proposed designed, modeled, and computationally simulated. This compressor can be matched with a properly designed nonlinearly chirped fiber Bragg grating stretcher to produce ultra-short high-peak-power laser pulses in a chirped pulsed laser amplification system. The major contributions of this thesis are summarized in Section 5.1, while some possible future work is discussed in section 5.2.

5.1 Summary

The major contribution of this thesis is the invention of a compact and robust monolithic optical pulse compressor (Figure 5.1). The distinguishing advantage of this compressor other than volume reduction is the reduction of its transverse size, or in other words, the grating size. This invention was inspired by the obstacle that conventional compressors face where gratings with large and uniformly ruled areas are difficult to fabricate, making it impossible for laser systems to move to the next level in higher energy delivery with previous compressor embodiments.

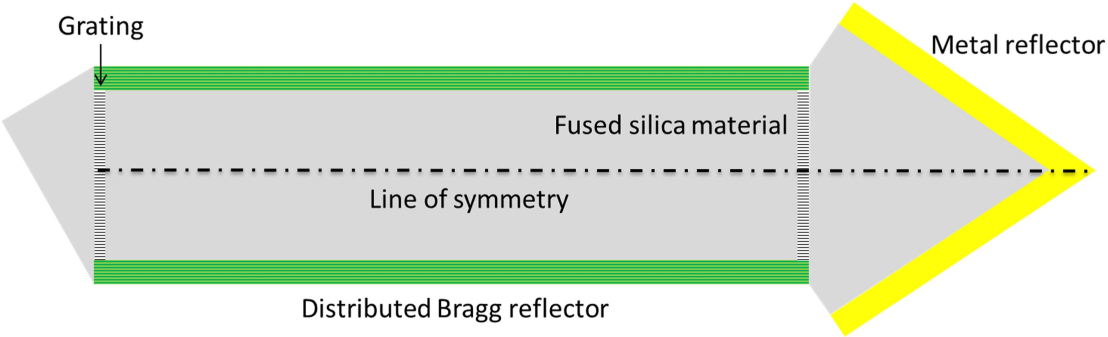

Figure 5.1 Proposed ultra-compact grating-based monolithic optical pulse compressor.

Folding the transverse size requires either mirrors or reflecting coatings. Mirrors can stand separately with other optical elements in a compressor, but require additional alignment effort. Thus reflecting coatings are chosen, and solid yet optically transparent material is filled into the space inside compressor. The solid material not only provides surfaces on which reflecting coatings can be deposited, but also integrates the compressor system into a single monolithic structure. Moreover, because it has a refractive index larger than that of air, the longitudinal size of the compressor is also reduced compared to conventional systems with air in them.

The pulse compression effects in the monolithic compressor can be calculated using a modified ray-tracing method. The first grating in the compressor serves the function of diffracting different wavelength components of the input pulse to different angular directions, while the second grating re-collimates the diffracted beams to parallel beams while also fixing the group velocity dispersion at a certain amount. So by choosing the compressor dimensions, the corresponding amount of dispersion is also automatically chosen. By adjusting the dimensional parameters of the compressor, different compression ratios can be achieved.

Quantitative calculations only provide the relationship of the input and output pulse durations for a given set of compressor parameters. The details of the output pulse cannot be determined. To appreciate the operation of the compressor, we used the finite-difference time-domain (FDTD) method to write a simulation program to simulate the response of the compressor to a chirped input pulse. The results of the electric field plots and output pulse shapes agree with the theoretical derivations. An input Gaussian pulse is successfully compressed; we also uncover that the saw-tooth-like optical path additions of the compressor causes a depression in the form of the output pulse. When paired with a properly designed nonlinearly chirped fiber Bragg grating pulse stretcher, the depression can be compensated for, and clean, ultra-short high-peak-power laser pulses can be produced.

The results obtained from numerical simulations provide us with guidance on how to make the actual device. Since the fabricated device usually cannot have the perfect parameters, there are mainly two aspects that need special attention when mechanical tolerance is considered. One is the incidence angle. When the rear mirrors are fixed, and the incidence angle is adjusted gradually around its desired value (59.13 degrees), we find that the tolerance for the incident angle is 1.15 degrees (2%). This gives maximum energy drop of 20% in the output, corresponding to an overall compressor efficiency of over 70% when anti-reflection schemes are properly applied.

In the simulation, the distributed Bragg reflector is considered ideal. In an experimental implementation, it should be carefully designed to provide high reflectivity in the desired wavelength operating band and incidence angle. A DBR is formed by multiple layers of alternating materials with different refractive indices. When the layer thickness is close to a quarter of the incident wavelength, light is forbidden to pass through the structure, and the reflectivity for the DBR is often higher than 99.5%. The stopband for a DBR is determined by the contrast in refractive index of the two materials forming the structure [35]. For a central wavelength of 1030 and contrast refractive index of 2.5 to 1, the stopband is as wide as 581 nm.

When the incidence direction is not normal, the reflectivity profile still has the same shape, but it is slightly shifted to the shorter wavelength direction. Thus as long as the layer depth is one quarter of the central wavelength, and the contrast of material is high enough, the DBR should be able to provide a reflectivity efficiency higher than 99%.

The compressor design should be adjusted according to a specific application. If only robustness is the primary concern, then the simple version of the monolithic compressor will serve the purpose. If both volume reduction and robustness are required, then the transverse size of the compressor (the grating size) should be reduced as much as possible, just to be able to include the input beam. This could be accomplished by making the width of the beam divergence to be multiple times of the grating width.

5.2 Future work

This document has presented a comprehensive research on the properties of a monolithic compressor, and its response to a stretched input pulse. The major remaining work to be done is to fabricate the compressor, and experimentally validate its operation.

Since the monolithic compressor is designed for portable and robust systems, it does not require alignment after fabrication. This in turn means that the monolithic compressor structure is difficult to change after fabrication. Thus to ensure best performance, the prototype version of the compressor should be tested first. The prototype version of the compressor basically consisted of three parts: two diffraction gratings, two side mirrors for folding the transverse size of the beam, and two rear mirrors for retro-reflecting the input pulse (Figure 5.2).

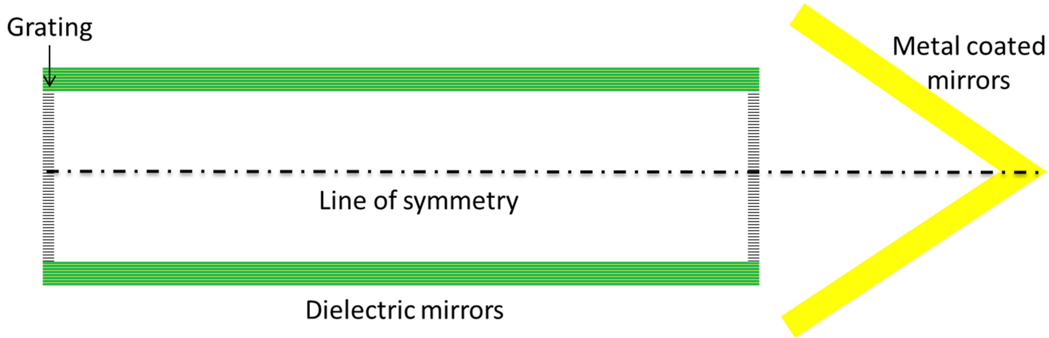

Figure 5.2 Reduced version of proposed optical pulse compressor.

When the prototype version is fabricated and tested, its parameters can be adjusted, and until optimal values are reach. These can then be used to fabricate the final device. Parameter tuning can be done for instance, by adjusting the incident pulse angle, or tilting the angles of the rear mirrors, until optimal values are obtained. The relative positions of the side dielectric mirrors and the diffraction gratings can also be tuned. After the best composition of parameters is arrived at, measured parameter results can be recorded so these can be used in the fabrication of monolithic compressor. By this iterative process, a precise monolithic compressor can be fabricated and implemented in a portable and robust chirped pulsed laser amplification system.

Reference

[1] Cook, Charles E. "Pulse compression-key to more efficient radar transmission." Proceedings of the IRE 48.3 (1960): 310-316.

[2] Treacy, E. B. "Compression of picosecond light pulses." Physics Letters A 28.1 (1968): 34-35.

[3] Treacy, Edmond. "Optical pulse compression with diffraction gratings." Quantum Electronics, IEEE Journal of 5.9 (1969): 454-458.

[4] Martinez, O. E., J. P. Gordon, and R. L. Fork. "Negative group-velocity dispersion using refraction." JOSA A 1.10 (1984): 1003-1006.

[5] Martinez, Oscar Eduardo. "3000 times grating compressor with positive group velocity dispersion: Application to fiber compensation in 1.3-1.6 μm region." Quantum Electronics, IEEE Journal of 23.1 (1987): 59-64.

[6] Strickland, Donna, and Gerard Mourou. "Compression of amplified chirped optical pulses." Optics communications 55.6 (1985): 447-449.

[7] Maine, P., D. Strickland, P. Bado, M. Pessot, and G. Mourou. "Generation of ultrahigh peak power pulses by chirped pulse amplification." IEEE Journal of Quantum electronics 24, no. 2 (1988): 398-403.

[8] Eidam, Tino, et al. "Femtosecond fiber CPA system emitting 830 W average output power." Optics letters 35.2 (2010): 94-96.

[9] Richardson, D. J., J. Nilsson, and W. A. Clarkson. "High power fiber lasers: current status and future perspectives [Invited]." JOSA B 27.11 (2010): B63-B92.

[10] Limpert, Jens, et al. "High-average-power femtosecond fiber chirped-pulse amplification system." Optics letters 28.20 (2003): 1984-1986.

[11] Gérôme, Frédéric, et al. "Delivery of sub-100fs pulses through 8m of hollow-core fiber using soliton compression." Optics express 15.12 (2007): 7126-7131.

[12] Gallmann, Lukas, et al. "Comparison of the filamentation and the hollow-core fiber characteristics for pulse compression into the few-cycle regime." Applied Physics B 86.4 (2007): 561-566.

[13] Chen, Xiaowei, et al. "Generation of 4.3 fs, 1 mJ laser pulses via compression of circularly polarized pulses in a gas-filled hollow-core fiber." Optics letters 34.10 (2009): 1588-1590.

[14] Travers, John C., et al. "Ultrafast nonlinear optics in gas-filled hollow-core photonic crystal fibers [Invited]." JOSA B 28.12 (2011): A11-A26.

[15] Wang, Y. Y., et al. "Design and fabrication of hollow-core photonic crystal fibers for high-power ultrashort pulse transportation and pulse compression." Optics letters 37.15 (2012): 3111-3113.

[16] Eggleton, Benjamin J., et al. "Experimental demonstration of compression of dispersed optical pulses by reflection from self-chirped optical fiber Bragg gratings." Optics letters 19.12 (1994): 877-879.

[17] Mokhtar, M. R., et al. "Fibre Bragg grating compression-tuned over 110 nm." Electronics Letters 39.6 (2003): 1.

[18] Broderick, N. G. R., et al. "Optical pulse compression in fiber Bragg gratings." Physical review letters 79.23 (1997): 4566.

[19] Kafka, J. D., and T. Baer. "Prism-pair dispersive delay lines in optical pulse compression." Optics

letters 12.6 (1987): 401-403.

[20] Imeshev, G., I. Hartl, and M. E. Fermann. "Chirped pulse amplification with a nonlinearly chirped fiber Bragg grating matched to the Treacy compressor." Optics letters 29.7 (2004): 679-681.

[21] Galvanauskas, A., et al. "All‐fiber femtosecond pulse amplification circuit using chirped Bragg gratings." Applied physics letters 66.9 (1995): 1053-1055.

[22] Sung, J. H., et al. "Generation of 0.2-TW 5.5-fs optical pulses at 1 kHz using a differentially pumped hollow-fiber chirped-mirror compressor." Applied Physics B 82.1 (2006): 5-8.

[23] Park, Juyun, Jae-hwan Lee, and Chang Hee Nam. "Generation of 1.5 cycle 0.3 TW laser pulses using a hollow-fiber pulse compressor." Optics letters 34.15 (2009): 2342-2344.

[24] Braun, Alan, Christopher Horvath, and Xinbing Liu. "Stretcher-compressor assembly having a single grating." U.S. Patent No. 6,081,543. 27 Jun. 2000.

[25] Shverdin, M. Y., et al. "Chirped-pulse amplification with narrowband pulses." Optics letters 35.14 (2010): 2478-2480.

[26] Lai, Ming, Shui T. Lai, and Casimir Swinger. "Single-grating laser pulse stretcher and compressor." Applied optics 33.30 (1994): 6985-6987.

[27] Shank, C. V., et al. "Compression of femtosecond optical pulses." Applied Physics Letters 40.9 (1982): 761-763.

[28] Tomlinson, W. J., R. H. Stolen, and C. V. Shank. "Compression of optical pulses chirped by self-phase modulation in fibers." JOSA B 1.2 (1984): 139-149.

[29] Clausnitzer, Tina, et al. "Highly efficient transmission gratings in fused silica for chirped-pulse amplification systems." Applied optics 42.34 (2003): 6934-6938.

[30] Wang, Shyh. "Principles of distributed feedback and distributed Bragg-reflector lasers." Quantum Electronics, IEEE Journal of 10.4 (1974): 413-427.

[31] McMullen, J. D. "Analysis of compression of frequency chirped optical pulses by a strongly dispersive grating pair." Applied optics 18.5 (1979): 737-741.

[32] Yee K. S., “Numerical solution of initial boundary value problems involving Maxwell's equations in isotropic media,” IEEE Transactions on Antennas and Propagation, 14, (1966), 302–307.

[33] Schneider, J. B., “Introduction to the Finite Difference Time-Domain method,” Lecture materials for EE 535, Chap. 3, WSU, 2007, pp. 34-35.

[34] Chang Yang, and Elias Towe. "Ultra-compact grating-based monolithic optical pulse compressor for laser amplifier systems." JOSA B 33.10 (2016): 2135-2143.

[35] Sheppard, C. J. R. "Approximate calculation of the reflection coefficient from a stratified medium." Pure and Applied Optics: Journal of the European Optical Society Part A 4.5 (1995): 665.

[36] Jae Hyoung Ryu, Hee Yun Kim, Hyun Kyu Kim, Yashpal Singh Katharria, Nam Han, Ji Hye Kang, Young Jae Park, Min Han, Beo Deul Ryu, Kang Bok Ko, Eun-Kyoung Suh, Chang-Hee Hong, "High performance of InGaN light-emitting diodes by air-gap/GaN distributed Bragg reflectors," Opt. Express 20, 9999-10003 (2012).